Joule

CellPress

Article

A Printable Organic Cathode Interlayer Enables over 13% Efficiency for 1-cm^2 Organic Solar Cells

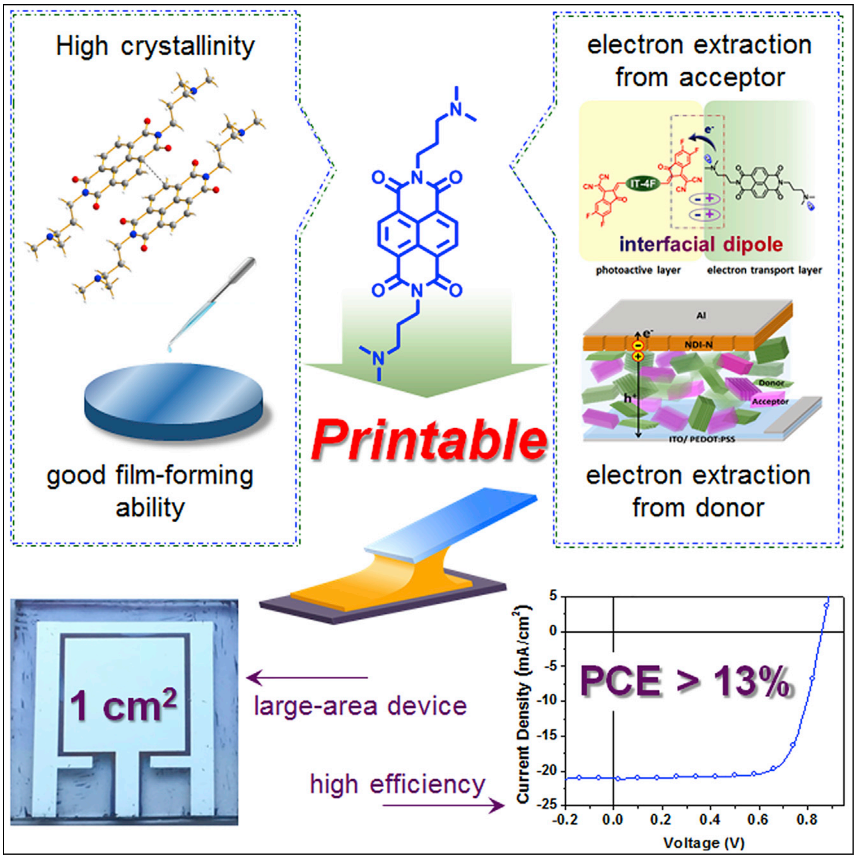

A naphthalene diimide (NDI)-based organic molecule (NDI-N) was prepared to be used as printable cathode interlayer (CIL) for organic solar cells (OSCs). NDI-N possesses combined advantages of high crystallinity and good film-forming properties, endowing the material with excellent electron-transport properties and good processability. NDI-N can be processed by printing methods; in this case an OSC device of 1 cm^2 was fabricated by using blade-coated NDI-N and an efficiency of 13.2% was achieved, which represents the highest efficiency to date for large-area OSCs.

Qian Kang, Long Ye, Bowei Xu, ..., Huifeng Yao, Harald Ade, Jianhui Hou

xubowei2004@iccas.ac.cn (B.X.)
hjhzlz@iccas.ac.cn (J.H.)

HIGHLIGHTS

A printable cathode interlayer (CIL) for OSCs is demonstrated for the first time

The high crystallinity and good processablity makes the organic CIL printable

The highest photovoltaic efficiency of large-area OSCs is achieved

Kang et al., Joule 3, 1–13
February 20, 2019 © 2018 Elsevier Inc.
https://doi.org/10.1016/j.joule.2018.10.024

Please cite this article in press as: Kang et al., A Printable Organic Cathode Interlayer Enables over 13% Efficiency for 1-cm^2 Organic Solar Cells, Joule (2018), https://doi.org/10.1016/j.joule.2018.10.024

Joule

CellPress

Article

A Printable Organic Cathode Interlayer Enables over 13% Efficiency for 1-cm^2 Organic Solar Cells

Qian Kang,[1] Long Ye,[2] Bowei Xu,[1,*] Cunbin An,[1] Samuel J. Stuard,[2] Shaoqing Zhang,[1] Huifeng Yao,[1] Harald Ade,[2] and Jianhui Hou[1,3,*]

SUMMARY

Currently, most cathode interlayer (CIL) materials for organic solar cells (OSCs) cannot be processed by printing techniques, which severely limits their use in practical productions. Herein, we report a naphthalene diimide (NDI)-based small-molecular compound (*N,N*-dimethylamino)propyl naphthalene diimide (NDI-N) as printable CIL for OSCs. NDI-N exhibits a unique advantage that combines the merits of high crystallinity and good film-forming property in one material, endowing the semiconductor with excellent electron-transport properties and good processability. By using the NDI-N as CIL, a high power-conversion efficiency (PCE) of 13.9% was achieved in a PBDB-T-2F:IT-4F-based OSC device. More importantly, a large-area OSC device of 1 cm^2 was fabricated by using the blade-coated NDI-N CIL and an outstanding PCE of 13.2% was achieved, which represents the highest efficiency of large-area OSCs. The results in this work may pave the way for low-cost and mass production of OSCs.

INTRODUCTION

Organic solar cells (OSCs) have emerged as a promising renewable energy technology due to their advantages in fabricating lightweight and large-area devices through low-cost solution methods.[1–5] In the past two years the power-conversion efficiency (PCE) of OSCs has exceeded 14%, showing a bright prospect for practical applications.[6,7] At present, much attention focuses on manufacturing large-area OSCs by using printing techniques, believed to be crucial for the mass production.[8–10] So far, several photoactive materials as well as anode interlayer materials have been demonstrated to be processable by printing methods in fabricating efficient and large-area OSCs.[11,12] In contrast, owing to the low electron mobility, cathode interlayer (CIL) materials are very sensitive to the film thickness in modifying OSC devices, making them incompatible with large-area printing processes where certain thickness variation is unavoidable.[13–15] To date, only ZnO has been demonstrated as a successful example of a CIL that could be processed by a printing method in OSC fabrication.[16] Unfortunately, the PCE of the corresponding device was much lower than the efficiencies of state-of-the-art OSCs.[16] At present, the lack of printable CIL has greatly impeded the pace toward practical production of OSCs, and thus the development of a new CIL with high electron mobility is in urgent demand.

Among various *n*-type organic semiconductors, materials based on perylene diimide (PDI) and naphthalene diimide (NDI) show the most promising performance in OSCs due to their suitable energy levels and excellent electron-transport properties.[17–19]

Context & Scale

With the constantly enhanced photovoltaic efficiencies, as well as the advantages of low cost and light weight, organic solar cells (OSCs) exhibit a bright prospect for a new generation of renewable energy technology. For practical use, manufacturing large-area OSC devices by printing techniques is becoming critically important for the mass production of OSCs. However, the lack of printable cathode interlayer (CIL) materials has greatly impeded the pace toward practical production.

Here, we report an organic semiconductor possessing superior photoelectronic properties and good processablity, which is capable of serving as a printable CIL material. By using the printed CIL to make large-area devices, the highest photovoltaic efficiency for large-area OSCs was obtained, which paves the way for the commercialization and practical use of organic photovoltaics technology.

Please cite this article in press as: Kang et al., A Printable Organic Cathode Interlayer Enables over 13% Efficiency for 1-cm^2 Organic Solar Cells, Joule (2018), https://doi.org/10.1016/j.joule.2018.10.024

Compared with their PDI counterparts,[19,20] the NDI-based compounds possess higher optical transparency, making them more suitable in serving as charge-transport layer in OSCs.[21] Recently, a series of *n*-type self-doped conjugated polymers based on NDI were synthesized as CILs, and several outstanding PCEs were achieved in the OSCs by using the NDI-based CILs.[22,23] Due to the superior electron-transport properties, the NDI-based polymers exhibited an excellent thickness insensitivity in fabricating high-performance OSCs, implying their great potential for being processed by printing techniques.[24]

However, regarding molecular design, two conflicting factors between crystallinity and film-forming properties severely limits the development of NDI-based materials as printable CILs.[25] On the one hand, high crystallinity is essential to achieve superior charge-transport capacity for CILs, but the highly crystalline small molecules tend to aggregate during the film fabrication, resulting in a coarse film surface with pinholes;[26–28] this not only significantly deteriorates the device performance but also brings difficulties in processing CILs. On the other hand, NDI-based polymers exhibit improved film-forming properties; however, the low crystallinity and disordered molecular arrangement of polymers reduce their charge-transport capacity, restricting their further application in OSCs. To date these key problems have not been solved, thus limiting the use of NDI-based semiconductors for mass productions of OSCs. Although many reports demonstrate that a minor structural modification can drastically improve the performance of organic semiconductors,[29,30] it is still a great challenge to develop NDI-based compounds that combine the merits of high crystallinity and good film-forming properties.

Here we report an organic molecule based on naphthalene diimide, namely (*N*,*N*-dimethylamino)propyl naphthalene diimide (NDI-N), as a printable CIL for OSCs. NDI-N exhibits a unique advantage that combines the merits of high crystallinity and good film-forming properties in one material. By comparison of NDI-N and (*N*,*N*-dimethyl-*N*-ethylammonium)propyl naphthalene diimide (NDI-Br), an NDI-N analog modified with quaternary ammonium salt, it is found that NDI-N can efficiently extract electrons from both the non-fullerene acceptor and the polymer donor, which is superior to most currently used CILs. Using the NDI-N as CIL, OSCs with different photoactive layers all exhibit the best device performance in comparison with their highest values in related reports. More importantly, NDI-N can be processed by a printing method for making large-area devices; i.e., a large-area OSC device of 1 cm^2 was fabricated by using blade-coated NDI-N CIL and an outstanding PCE of 13.2% was achieved. To the best of our knowledge, this is the highest efficiency to date for large-area OSCs.

RESULTS AND DISCUSSION

The synthetic procedures of NDI-N and NDI-Br are illustrated in Figure 1A. NDI-N was prepared by a simple one-step reaction from commercially available compounds, 1,4,5,8-naphthalenetetracarboxylic dianhydride and *N*,*N*-dimethyl-1,3-propane-diamine, and was readily purified by recrystallization in ethanol, affording the lamellar crystal with a yield of 80%.[31] The ammonium-functionalized NDI-Br was synthesized by quaternizing the precursor compound NDI-N with excess bromoethane in *N*,*N*-dimethylformamide (DMF).[32] The molecular structures of NDI-N and NDI-Br were confirmed by ^{1}H nuclear magnetic resonance, MALDI-TOF with mass spectrometry, electrospray ionization mass spectrometry (Figure S1), and elemental analysis (Table S1). Both NDI-N and NDI-Br can be dissolved in polar organic solvents such as methanol, dimethylsulfoxide, and DMF. Figure 1B shows

[1]State Key Laboratory of Polymer Physics and Chemistry, Beijing National Laboratory for Molecular Sciences, Institute of Chemistry Chinese Academy of Sciences, Beijing 100190, P.R. China

[2]Department of Physics Organic and Carbon Electronics Lab (ORaCEL), North Carolina State University, Raleigh, NC 27695, USA

[3]Lead Contact

*Correspondence:
xubowei2004@iccas.ac.cn (B.X.),
hjhzlz@iccas.ac.cn (J.H.)

https://doi.org/10.1016/j.joule.2018.10.024

Please cite this article in press as: Kang et al., A Printable Organic Cathode Interlayer Enables over 13% Efficiency for 1-cm^2 Organic Solar Cells, Joule (2018), https://doi.org/10.1016/j.joule.2018.10.024

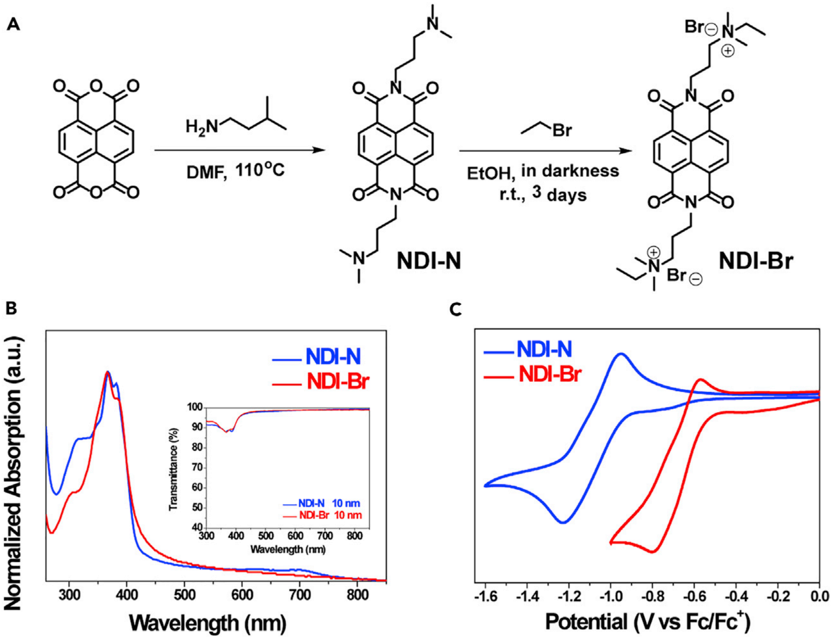

Figure 1. Chemical Synthesis and Photophysical Characterizations

(A) Synthetic route of NDI-N and NDI-Br.

(B) Normalized UV-vis absorption spectra of NDI-N and NDI-Br films. The inset is their transmittance spectra.

(C) Cyclic voltammograms of NDI-N and NDI-Br films on glassy carbon electrodes in 0.1 M Bu_4NPF_6 in acetonitrile solution at a scan of 20 mV/s.

the absorption spectra of NDI-N and NDI-Br as solid films, and the inset provides their transmittance spectra. The absorption maxima at 368 nm are ascribed to the π-π^* transition of the NDI unit, while the broad absorption tails from 450 to 750 nm can be assigned to the polaronic transition ($\lambda_{polaron}$), indicating the self-doping effect of the two compounds. Moreover, the high transmittance (over 98%) of the NDI-N and NDI-Br films in the long-wavelength region from 450 to 800 nm avoids the negative effect on the light-harvesting of photoactive layers. Cyclic voltammetry measurements were conducted to evaluate the molecular energy levels of NDI-N and NDI-Br. On the basis of the onset reduction potentials, the lowest unoccupied molecular orbital (LUMO) levels of NDI-N and NDI-Br were determined to be −3.98 and −3.69 eV, respectively (Figure 1C). The low-lying LUMO level of NDI-N is favorable to the electron extraction and transport of CILs. As reported in previous studies, when the LUMO level of CIL is lower than that of the acceptor, a charge can be injected into the CIL without energy barrier and subsequently be transported within the CIL film.[33] In this case, a large thickness window of CIL can be applied to achieve high OSC performances, which is one of critical requirements for the CIL to be processed by printing methods.

Crystallinity and molecular arrangement have important influences on the electron-transport properties of organic semiconductors. We first utilized single-crystal X-ray analysis to investigate the effect of molecular packing on the charge-transport property of NDI-N, as shown in Figures 2A and 2B. There are two molecules per unit cell in the $P\bar{1}$ space group, and each molecule is located on an inversion center. The NDI-N molecules in the lattice exhibit a tilted parallel π-stacking arrangement, and the distances between the packing layers are 3.3 Å. The intermolecular π-π packing distance of NDI-N is among the shortest π-planar distances of NDI-based

Please cite this article in press as: Kang et al., A Printable Organic Cathode Interlayer Enables over 13% Efficiency for 1-cm^2 Organic Solar Cells, Joule (2018), https://doi.org/10.1016/j.joule.2018.10.024

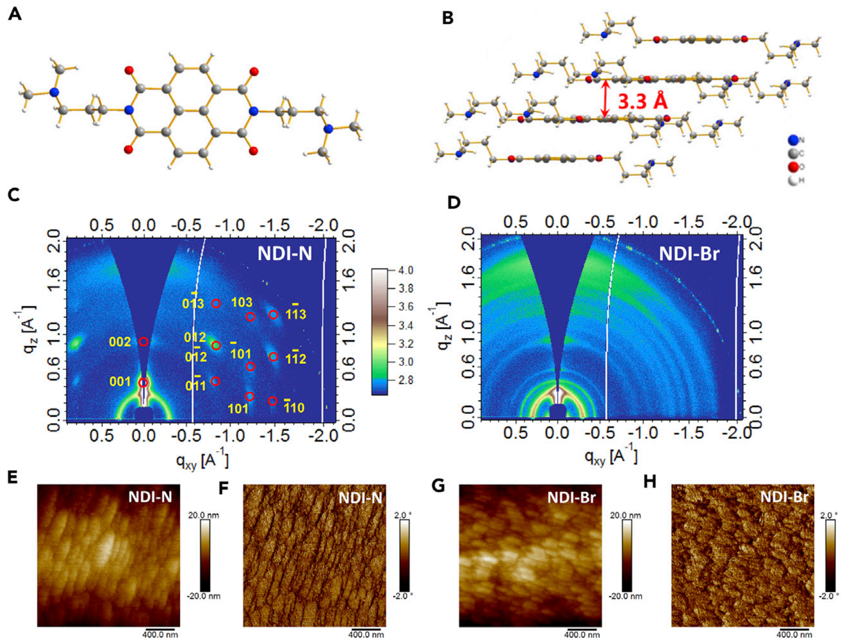

Figure 2. Crystal Structures and Film-Forming Properties of NDI-Based Molecules

(A) Molecular structure of NDI-N.

(B) Crystal π-stacking view of NDI-N.

(C and D) 2D GIWAXS patterns for NDI-N (C) and NDI-Br films deposited on the photoactive layer (D). The incident angle (0.08°) is well below the critical angle (~0.13°) of the PBDB-T-2F:IT-4F blend film.

(E–H) AFM topography (E and G) and phase images (F and H) of NDI-N and NDI-Br films deposited on the photoactive layer.

molecules reported previously.[34–37] The compact π-planar packing of NDI-N is beneficial for enhancing the charge transport. Moreover, grazing-incidence wide-angle X-ray scattering (GIWAXS)[38] was used to measure the neat NDI-N and NDI-Br films deposited on silicon substrates. As can be seen from Figure S2, the NDI-N film exhibits well-defined and pronounced diffraction spots, indicating a high degree of crystalline order. By contrast, the NDI-Br film showed only some weak and irregular diffraction spots, implying a less ordered nature of the film. To probe the actual microstructure of these interlayers in OSC devices, we further studied the NDI-N and NDI-Br films deposited on the photoactive layer by gradually increasing the incident angle from 0.05° to 0.20°. The angle dependence of these samples is shown in Figures S3 and S4. Figures 2C and 2D respectively present the 2D GIWAXS patterns of NDI-N and NDI-Br films deposited on the top of the photoactive layer with a small incident angle of 0.08°, which yield a consistent trend that NDI-N is much more ordered than NDI-Br. By combination with single-crystal X-ray analysis, all the diffraction peaks in the 2D GIWAXS pattern have been indexed,[39] and the (001) plan can be defined as parallel orientation to the substrate. The mean size of the crystallites was acquired through calculating the crystal coherence length (CCL) using the Scherrer equation. The CCL of NDI-N was 10.4 nm, indicating a high ordering of the NDI-N film. As reported in previous works, the highly crystalline molecules tend to aggregate during the film fabrication, resulting in a coarse film surface with numerous pinholes; this not only severely deteriorates the device performance but also brings difficulties in processing CILs. However, as shown in Figures 2E and 2F, the atomic force microscopy (AFM) images of the NDI-N film deposited on the photoactive layer exhibit a smooth and uniform surface with a low root-mean-square roughness (R_q) value of 4.23 nm, indicating that the highly crystalline NDI-N can also

Please cite this article in press as: Kang et al., A Printable Organic Cathode Interlayer Enables over 13% Efficiency for 1-cm^2 Organic Solar Cells, Joule (2018), https://doi.org/10.1016/j.joule.2018.10.024

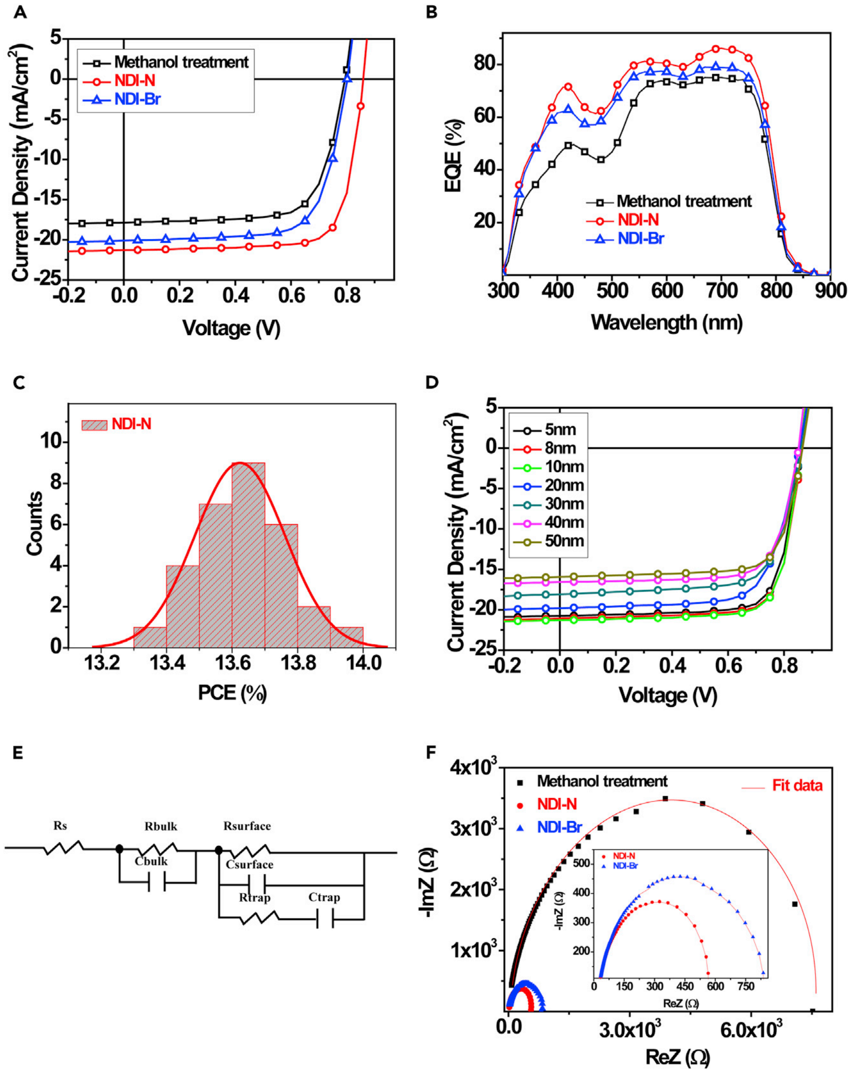

Figure 3. Photovoltaic Parameters of Devices and Electrochemical Impedance Spectroscopy

(A and B) *J-V* (A) and EQE (B) curves of the best-performing NDI-N and NDI-Br-based devices.

(C) Histograms of the PCE counts for 30 individual NDI-N-based cells.

(D) *J-V* curves of the OSC devices with various NDI-N thicknesses.

(E) The equivalent-circuit model employed for EIS fitting of the devices.

(F) Nyquist plots of different CIL film-modified devices.

form desirable films. Based on these results, it can be suggested that the high crystallinity and compact molecular packing is beneficial in improving the electron-transport properties of NDI-N which, in combination with good film-forming property, is the key factor for NDI-N to be processed by printing methods.

To evaluate the performance of the NDI-based compounds as CILs in OSCs, we fabricated conventional devices with the configuration of indium tin oxide (ITO)/poly(3,4-ethylenedioxythiophene) polystyrene sulfonate (PEDOT:PSS)/photoactive layer/NDI-based CIL/Al. Here, a blend based on a polymer donor, PBDB-T-2F, and a non-fullerene acceptor, IT-4F, is used as the photoactive material. For comparison, devices with PFN-Br, ZnO nanoparticles (NPs), and methanol treatment were also fabricated as a control. The current density-voltage (*J-V*) characteristics of the devices and relevant parameters are shown in Figure 3A and Table 1, respectively,

Please cite this article in press as: Kang et al., A Printable Organic Cathode Interlayer Enables over 13% Efficiency for 1-cm^2 Organic Solar Cells, Joule (2018), https://doi.org/10.1016/j.joule.2018.10.024

Table 1. Photovoltaic Parameters of Conventional Devices with NDI-N, NDI-Br, and Methanol Treatment and Inverted Device with NDI-N under the Illumination of AM 1.5G, 100 mW cm^{-2}

Devices	V_{oc} (V)	J_{sc} (mA/cm^2)	FF	PCE (%)	J_{cal}[a] (mA/cm^2)	R_s (Ω cm^2)	R_{sh} (kΩ cm^2)
Methanol treatment	0.79	17.9	0.71	10.1	17.3	5.39	1.23
NDI-N	0.86	21.3	0.76	13.9	20.6	2.66	1.85
NDI-Br	0.80	20.1	0.71	11.5	19.4	3.77	0.74
Inverted device (NDI-N)	0.83	21.5	0.71	12.6	20.8	3.53	1.46

[a] Integrated J_{cal} from the EQE curves.

with the external quantum efficiency (EQE) curves displayed in Figure 3B. The optimal thickness was found to be 10 nm for both NDI-N and NDI-Br. The OSC device modified by NDI-N delivered the best PCE of 13.9%, along with a short-circuit current density (J_{sc}) of 21.3 mA/cm^2, an open-circuit voltage (V_{oc}) of 0.86 V, and a fill factor (FF) of 0.76, which is higher than that of the PBDB-T-2F:IT-4F-based device in the most recent report using PFN-Br.[40] Figure 3C presents a PCE histogram of 30 NDI-N-modified devices; over 60% of the devices exhibit PCE values exceeding 13.6%, indicating the good reproducibility of the NDI-N-modified OSCs. For the devices with PFN-Br, ZnO NPs, NDI-Br, and methanol treatment, the PCEs of the devices are 13.5%, 13.1%, 11.5%, and 10.1%, respectively. Electrochemical impedance spectroscopy (EIS) measurements were performed to examine the interface resistance of the devices. Figure 3F shows Nyquist plots of NDI-N-modified devices in the dark. A bias voltage equal to V_{oc} was applied to dissipate the total current.[41] The data were fitted using the equivalent-circuit model from a previous report,[42] and the corresponding results are listed in Table S4. The surface resistance ($R_{surface}$) of the devices with NDI-N, NDI-Br, PFN-Br, ZnO NPs, and methanol treatment was estimated to be 586.6, 884.2, 359.3, 751.8, and 6,475 Ω, respectively. The $R_{surface}$ of fullerene-free devices can be significantly decreased by using NDI-N CILs, indicating the reduced charge recombination and improved charge extraction in the NDI-N-modified OSCs. The stability of devices modified with NDI-N, NDI-Br, PFN-Br, and ZnO NPs was tested under ambient conditions (Figure S9). PCEs of devices modified with NDI-N, NDI-Br, and PFN-Br CILs can retain 83%, 83%, and 86% of their initial PCE values after 20 days, respectively, whereas the PCE of ZnO NPs-modified device declines to 38% of its initial value.

Furthermore, NDI-N was employed for modifying other efficient active layers, including PBDB-T:ITIC, DRTB-T:IDIC, and PBDB-T:IT-M. The *J-V* curves of these devices are provided in Figure S10, and the corresponding photovoltaic parameters are summarized in Table 2. All the devices exhibited PCEs comparable with their highest values in related reports,[43–45] indicating that NDI-N is a universal and effective CIL for various active layers. Moreover, due to its high transparency, NDI-N was used to fabricate inverted devices with a configuration of ITO/NDI-N/PBDB-T-2F:IT-4F/MoO$_3$/Al, whereby a PCE of 12.6% was achieved (Figure S11 and Table 1). These results suggest that NDI-N is a promising CIL material for various applications in OSCs. We further investigated the effect of NDI-N and NDI-Br thicknesses on the OSC performances. As shown in Figure 3D and Table S2, NDI-N exhibits an outstanding tolerance to thickness variation in fabricating OSCs; i.e., when the NDI-N thickness changed from 5 to 30 nm, the PCE remained at over 11.6%. It is worth noting that the R_s remains almost unchanged and the FF maintains a high value of 0.74 when the NDI-N thickness increases to 50 nm, indicating the excellent electron-transport and collection properties of NDI-N. The excellent thickness

Please cite this article in press as: Kang et al., A Printable Organic Cathode Interlayer Enables over 13% Efficiency for 1-cm^2 Organic Solar Cells, Joule (2018), https://doi.org/10.1016/j.joule.2018.10.024

Table 2. Photovoltaic Parameters of Devices Based on NDI-N Films with Different Photoactive Layers

Active Layer	CIL	V_{oc} (V)	J_{sc} (mA/cm^2)	FF	PCE (%)	J_{cal}[a] (mA/cm^2)
PBDB-T:ITIC	NDI-N	0.90	17.4	0.69	10.9	16.1
	NDI-Br	0.84	17.0	0.62	8.87	15.8
PBDB-T:IT-M	NDI-N	0.94	16.9	0.71	11.3	16.1
	NDI-Br	0.88	16.4	0.64	9.29	15.1
DRTB-T:IDIC	NDI-N	0.98	15.5	0.60	9.10	15.3
	NDI-Br	0.94	14.8	0.53	7.44	14.6

[a] Integrated J_{cal} from the EQE curves.

insensitivity of NDI-N for modifying OSCs is crucial for processing the CIL by printing methods. In contrast, the PCEs of the devices modified by NDI-Br, ZnO NPs, and PFN-Br dramatically decreased to 5.20%, 7.88%, and 4.08%, respectively, as the CIL thickness increased to 30 nm (Figure S7 and Table S3).

In an OSC device, the CIL contacts either the electron donor or the electron acceptor at the photoactive layer/CIL interface; therefore, an ideal CIL can extract electrons from both the donor and the acceptor. In previous works, the doping interaction between CILs and PCBM ([6,6]-phenyl-C_{61}-butyric acid methyl ester) has been proved to facilitate the electron extraction of fullerene-based devices;[46] however, doping on non-fullerene acceptors has not yet been reported. Here, electron spin resonance (ESR) spectroscopy was performed to investigate the doping effects of NDI-based molecules. First, the self-doping effect of the NDI-based small molecules can be confirmed by the ESR signals related to delocalized polarons that are observed in the neat NDI-N and NDI-Br films (Figure 4A), which is consistent with the results of UV-visible (UV-vis) absorptions. Second, a much stronger resonance peak with g values of 31.16 is detected in the NDI-N:IT-4F blend, confirming that the non-fullerene acceptor IT-4F can be effectively doped by NDI-N. In contrast, only a moderate ESR signal was observed in the NDI-Br:IT-4F blend because of the self-doping behavior of NDI-Br, suggesting that the doping effect of NDI-Br on IT-4F could be excluded. Lewis basicity can be used to elucidate the different n-doping behaviors of the two blends.[47] Compared with Br^-, the Lewis basicity of the amine group is much stronger, and thus the electron transfer from NDI-N to IT-4F is more efficient, resulting in significant n-doping of IT-4F. As a result, the electron transfer from NDI-N to IT-4F may induce an interfacial dipole layer at the IT-4F/NDI-N interface (Figure 4B), which facilitates electron extraction from the active layer to the cathode.

To verify the above inference, we fabricated electron-only devices with the configuration ITO/ZnO/IT-4F/NDI-N or NDI-Br/Al. Under a reverse bias voltage ranging from −2 to 0 V, at which electrons were injected from ITO and collected by the Al electrode, the current density of the NDI-N-based device is 6-fold higher than that of the NDI-Br-based device (Figure 4C), suggesting that doping on non-fullerene acceptor can facilitate the electron extraction at the photoactive layer/CIL interface. Moreover, doping on the non-fullerene acceptor could effectively improve the rectification characteristic of the device, which was demonstrated by fabricating p-n junction diodes with a structure of ITO/PEDOT:PSS/IT-4F/NDI-based compound (20 nm)/Al and measuring the *J-V* characteristics in the dark. As shown in Figure S13, the rectification ratio (the quotient of the current density at ±2 V) of the NDI-N-based diode is three times higher than that of the NDI-Br-based device, suggesting that the rectification characteristic of OSC devices can be effectively enhanced by doping the non-fullerene acceptor.

Please cite this article in press as: Kang et al., A Printable Organic Cathode Interlayer Enables over 13% Efficiency for 1-cm^2 Organic Solar Cells, Joule (2018), https://doi.org/10.1016/j.joule.2018.10.024

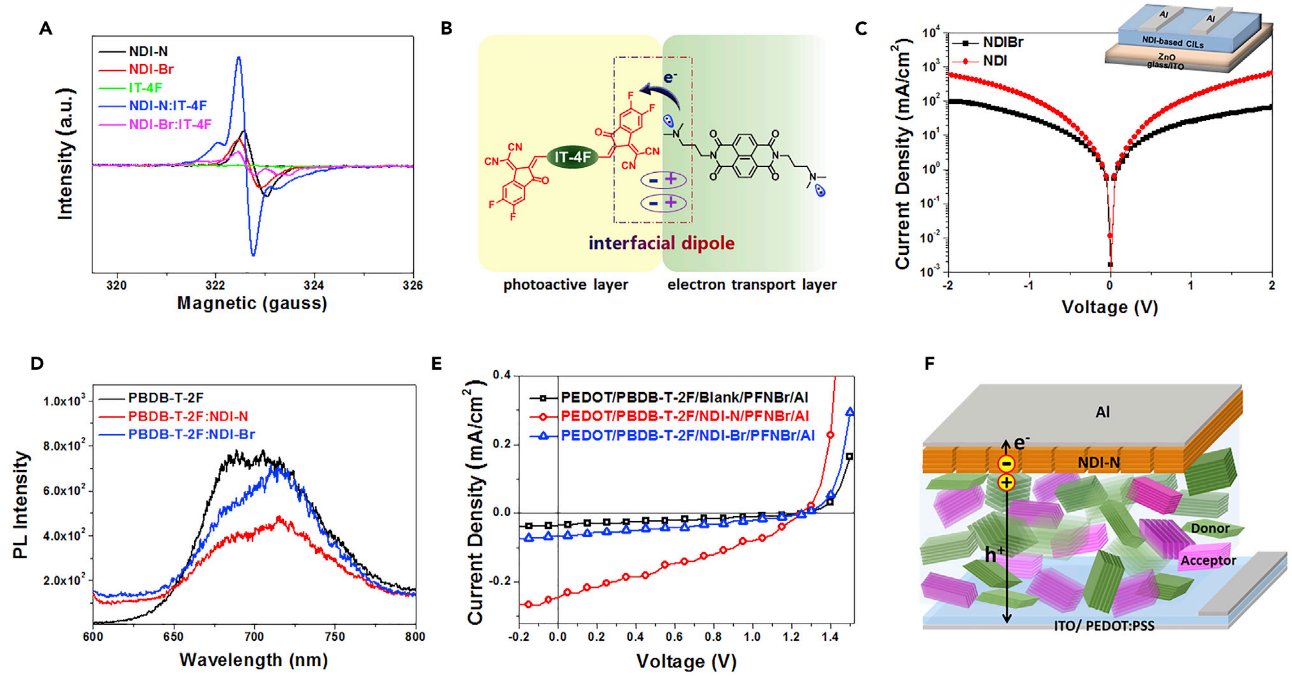

Figure 4. Characterizations of the Electron Extraction Capacity of NDI-N

(A) ESR spectra of the solid samples of NDI-N, NDI-Br, IT-4F, NDI-N:IT-4F, and NDI-Br:IT-4F.

(B) Schematic illustration of interfacial dipole formed by the doping between IT-4F and NDI-N.

(C) Semilogarithmic current density versus voltage characteristics of electron-only devices.

(D) PL spectra of PBDB-T-2F, PBDB-T-2F:NDI-N, and PBDB-T-2F:NDI-Br films.

(E) *J-V* curves of the bilayer heterojunction devices.

(F) Schematic illustration of exciton dissociation at the donor/NDI-N interface.

Furthermore, NDI-N can also extract electrons from polymer donors at the photoactive layer/CIL interface. As shown in Figure 4D, the photoluminescence (PL) emission (under excitation at 680 nm) of PBDB-T-2F was considerably quenched by NDI-N, whereas there was only a slight drop in the PL peak for the PBDB-T-2F:NDI-Br blend. The LUMO level of NDI-N is lower than that of PBDB-T-2F, which induces exciton dissociation at the contact interface between NDI-N and PBDB-T-2F (Figure S5). This result indicates that NDI-N can be used as an electron acceptor in devices. To demonstrate the contribution of NDI-N serving as electron acceptor to photocurrent generation, we fabricated bilayer devices with a configuration of ITO/PEDOT:PSS/PBDB-T-2F/NDI-N or NDI-Br/PFN-Br/Al. As shown in Figure 4E and Table S6, the PBDB-T-2F/NDI-N-based bilayer device showed an improved J_{sc} and an observable photovoltaic effect, suggesting that NDI-N can act as an electron acceptor under illumination. Based on these results, it can be concluded that in contrast to NDI-Br, NDI-N can efficiently extract electrons from both the polymer donor and the non-fullerene acceptor.

To demonstrate the compatibility of the CIL with printing techniques, we processed NDI-N by blade-coating to fabricate large-area OSCs (Figure 5A). The device architecture is the same as that used in the spin-coated devices, and the 1-cm^2 OSCs with ZnO NPs and PFN-Br CILs were also fabricated for comparison. As shown in Figure S15, a large-area NDI-N film of 1 cm^2 (1 cm × 1 cm) was fabricated through a blade-coating approach, and the AFM images of the NDI-N film were collected at different spots along the diagonal line of the film. All the collected AFM images exhibited smooth surfaces with low R_q values of about 2.2 nm, suggesting that the

Please cite this article in press as: Kang et al., A Printable Organic Cathode Interlayer Enables over 13% Efficiency for 1-cm^2 Organic Solar Cells, Joule (2018), https://doi.org/10.1016/j.joule.2018.10.024

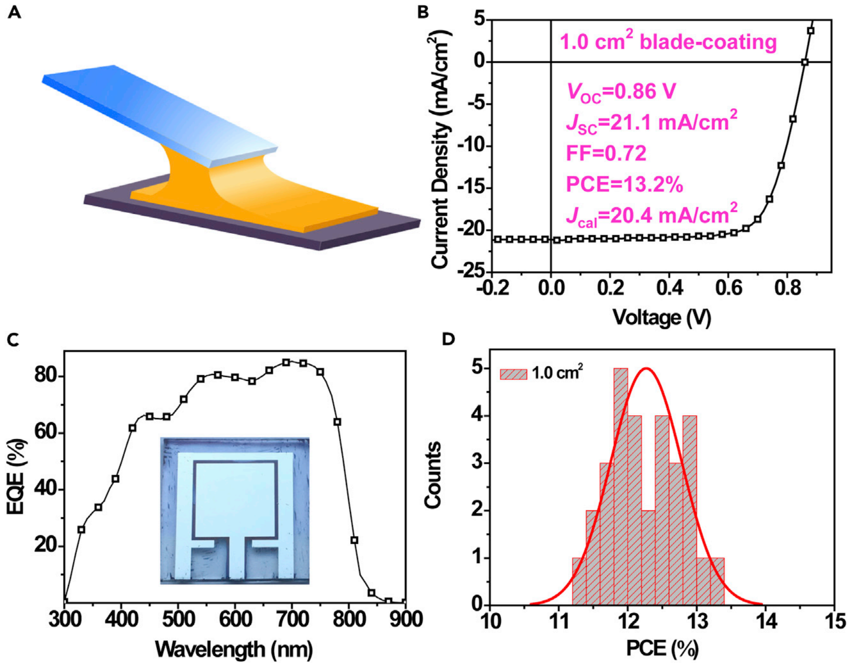

Figure 5. Fabrication and Device Performance of Large-Area OSCs

(A) Schematic illustration of blade-coating processes.

(B and C) *J-V* (B) and EQE (C) curves of devices using blade-coated NDI-N as CIL.

(D) Histograms of the PCE counts for 30 individual 1.0-cm^2 cells.

whole NDI-N film is smooth and uniform. The good wetting property of NDI-N methanol solution on the hydrophobic surface is favorable for making smooth and uniform CIL when printing the CIL on photoactive layers. As shown in Figure S16, the methanol solution drop was immediately spread with the contact angle close to 0° when it contacted the PBDB-T-2F:IT-4F surface, indicating the complete wetting of NDI-N solution on the photoactive layer. The good film-forming properties in combination with the excellent electron transport are favorable for processing NDI-N through printing methods. As shown in Figure 5B, the large-area OSC device of 1 cm^2 with the NDI-N CIL processed by the blade-coating exhibits an outstanding PCE of 13.2%. To the best of our knowledge, this is the highest efficiency reported thus far for large-area OSCs. The photovoltaic performance of the 0.81-cm^2 OSC (0.9 cm × 0.9 cm mask) was certified by the National Institute of Metrology (NIM), and a certified PCE of 12.20% was acquired (Figure S24). It is understandable that the lower PCE certified by the NIM is mainly derived from the slightly decreased J_{sc}. The J_{sc} in the certification is measured with the mask, which is lower than that of the unmasked case due to the non-negligible mask thickness compared with the aperture size. Figure 5D and Table S9 present a PCE histogram of 30 independent cells, in which more than 63% of the cells exhibited PCE values exceeding 12%. To make a comparison with the recent results of large-area devices, we carried out a survey (see Table 3) of state-of-the-art OSCs to date with an area of ca. 1 cm^2. Consequently, the PCE achieved in our work is the highest efficiency at present for large-area OSCs. Moreover, it is worth noting that the NDI-N thickness has little influence on PCEs of large-area devices. When the NDI-N concentration used in the blade-coating was increased from 0.1 to 1.0 mg/mL, the OSC with a thick NDI-N film only showed a moderate decline in PCE (Figure S17 and Table S10). In contrast, when the PFN-Br concentration changed from 0.1 to 1.0 mg/mL, the PCE of the device dramatically decreased from 5.76% to 4.09%. Compared with PFN-Br, the

Please cite this article in press as: Kang et al., A Printable Organic Cathode Interlayer Enables over 13% Efficiency for 1-cm^2 Organic Solar Cells, Joule (2018), https://doi.org/10.1016/j.joule.2018.10.024

Table 3. Survey of Photovoltaic Parameters of the State-of-the-Art Large-Area OSCs by Blade-Coating Techniques

Photoactive Layer	Device Area (cm^2)	PCE (%)	Year	Reference
PCDTBT:PC$_{71}$BM	0.64	4.9	2014	Smith et al.[48]
BDTT-S-TR:PC$_{71}$BM	1.44	6.7	2015	Cui et al.[49]
P3HT:PC$_{61}$BM	0.96	2.8	2015	Ye et al.[50]
PTZ1:IDIC	0.81	10.5	2017	Guo et al.[51]
PB-3T:IT-M	1.00	10.1	2018	Kang et al.[12]
PBTA-TF:IT-M	1.00	10.6	2018	Zhao et al.[11]
FTAZ:IT-M	0.56	9.8	2018	Ye et al.[3]
PBDB-T-2F:IT-4F	1.00	12.3 ± 0.9	2018	this work

superior electron transport of NDI-N is favorable for efficient electron collection when the thick NDI-N film is used. Moreover, ZnO NPs also exhibited considerable thickness sensibility in fabricating a 1-cm^2 device (Figure S18 and Table S10). AFM images showed that the thick ZnO NPs film exhibited a non-uniform surface with a high R_q of 5.39 nm, causing a large number of interfacial defects and reducing the FF of the device. Consequently, the large-area device with blade-coated ZnO NPs CILs only exhibits relatively low PCE of 8.89%.

The R_s (5.54 Ω cm^2) of 1-cm^2 OSCs is larger than that of the small-area device (2.66 Ω cm^2), which is indeed responsible for the slight decrease of J_{sc} and FF in the large-area device, while the R_{sh} for the large-area device (2.10 kΩ cm^2) is similar to that of the small-area device (1.85 Ω cm^2). Figure S19 presents the *J-V* characteristic of the large-area device in darkness. The current-leakage of 1-cm^2 OSC has no obvious increase as compared with the small-area device, which may explain the high FF in the large-area device. The small current-leakage implies that the interfacial defects can be suppressed in the large-area device by using the NDI-N CIL. To demonstrate the capacity of NDI-N in passivating defects or pinholes, we fabricated devices with the structure of ITO/PEDOT:PSS/NDI-N or PFN-Br/Al. As shown in Figure S20, the bilayer device with NDI-N exhibits a typical diode characteristic, suggesting that the contact point can still maintain a rectifying property for a selective charge collection even though NDI-N fills the pinholes in the photoactive layer and directly contacts the PEDOT:PSS. On the contrary, the PFN-Br-based device exhibits a linear *J-V* characteristic, implying that the defects or pinholes filled with PFN-Br only have non-selective charge transport. These results suggest that NDI-N can passivate defects or pinholes in photoactive layers, endowing the large-area device with high efficiency.

Conclusions

In conclusion, we reported an *n*-type NDI-based small-molecular semiconductor, NDI-N, as a printable CIL for high-performance OSCs. NDI-N exhibits a unique advantage of combining the merits of high crystallinity and good film-forming properties in one material, endowing the semiconductor with excellent electron-transport properties and good processability. By comparison of NDI-N with NDI-Br, we found that NDI-N can efficiently extract electrons from both the non-fullerene acceptor and the polymer donor. Due to the excellent electron transport and good processability, NDI-N can be processed by a printing method to make large-area devices; i.e., a large-area OSC device of 1 cm^2 was fabricated by using the blade-coated NDI-N CIL and an outstanding PCE of 13.2% was achieved. To the best of our knowledge, this is the highest efficiency thus far for large-area

OSCs. This work not only develops a small molecule with combined merits of high crystallinity and good film-forming properties, but also demonstrates a successful example of processing the CIL by a printing method for making large-area and high-performance OSC devices, which is of great significance for low-cost mass production of OSCs.

EXPERIMENTAL PROCEDURES

Full experimental procedures are provided in the Supplemental Information.

SUPPLEMENTAL INFORMATION

Supplemental Information includes Supplemental Experimental Procedures, 24 figures, and 10 tables and can be found with this article online at https://doi.org/10.1016/j.joule.2018.10.024.

ACKNOWLEDGMENTS

The authors acknowledge the financial support from the NSFC (21504095, 51373181) and the Chinese Academy of Science (XDB12030200, KJZD-EW-J01). L.Y. and H.A. were supported by the US Office of Naval Research (grant ONR, no. N000141712204). S.J.S. was supported by the National Science Foundation under grant no. DGE-1633587. Use of the beamline 7.3.3, Advanced Light Source was supported by the Director of the Office of Science, Office of Basic Energy Sciences, of the US Department of Energy under contract no. DE-AC02-05CH11231.

AUTHOR CONTRIBUTIONS

B.X. and J.H. proposed the research, directed the study, and analyzed the data. Q.K. carried out the device fabrication and characterizations. C.A. helped with X-ray single-crystal analysis. L.Y. and H.A. performed GIWAXS measurements. S.J.S. indexed the diffraction peaks in the GIWAXS measurements. H.Y. and S.Z. provided the photovoltaic materials. B.X., J.H., and Q.K. prepared the manuscript. B.X. and J.H. supervised the whole project. All authors discussed the results and commented on the manuscript.

DECLARATION OF INTERESTS

The authors declare no competing interests.

Received: August 30, 2018
Revised: October 12, 2018
Accepted: October 22, 2018
Published: November 15, 2018

REFERENCES

1. Heeger, A.J. (2014). 25th anniversary article: bulk heterojunction solar cells: understanding the mechanism of operation. Adv. Mater. *26*, 10–27.
2. Yu, G., Gao, J., Hummelen, J.C., Wudl, F., and Heeger, A.J. (1995). Polymer photovoltaic cells—enhanced efficiencies via a network of internal donor-acceptor heterojunctions. Science *270*, 1789–1791.
3. Ye, L., Xiong, Y., Zhang, Q., Li, S., Wang, C., Jiang, Z., Hou, J., You, W., and Ade, H. (2018). Surpassing 10% efficiency benchmark for nonfullerene organic solar cells by scalable coating in air from single nonhalogenated solvent. Adv. Mater. *30*, 1705485.
4. Song, W., Fan, X., Xu, B., Yan, F., Cui, H., Wei, Q., Peng, R., Hong, L., Huang, J., and Ge, Z. (2018). All-solution-processed metal-oxide-free flexible organic solar cells with over 10% efficiency. Adv. Mater. *30*, 1800075.
5. Diao, Y., Zhou, Y., Kurosawa, T., Shaw, L., Wang, C., Park, S., Guo, Y., Reinspach, J.A., Gu, K., Gu, X., et al. (2015). Flow-enhanced solution printing of all-polymer solar cells. Nat. Commun. *6*, 7955.
6. Zhang, S., Qin, Y., Zhu, J., and Hou, J. (2018). Over 14% efficiency in polymer solar cells enabled by a chlorinated polymer donor. Adv. Mater. *30*, 1800868.
7. Li, S., Ye, L., Zhao, W., Yan, H., Yang, B., Liu, D., Li, W., Ade, H., and Hou, J. (2018). A wide band gap polymer with a deep highest occupied molecular orbital level enables 14.2% efficiency in polymer solar cells. J. Am. Chem. Soc. *140*, 7159–7167.
8. Strohm, S., Machui, F., Langner, S., Kubis, P., Gasparini, N., Salvador, M., McCulloch, I., Egelhaaf, H.J., and Brabec, C.J. (2018). P3HT:

non-fullerene acceptor based large area, semi-transparent PV modules with power conversion efficiencies of 5%, processed by industrially scalable methods. Energy Environ. Sci. *11*, 2225–2234.

9. Søndergaard, R., Hösel, M., Angmo, D., Larsen-Olsen, T.T., and Krebs, F.C. (2012). Roll-to-roll fabrication of polymer solar cells. Mater. Today *15*, 36–49.

10. Sandstrom, A., Dam, H.F., Krebs, F.C., and Edman, L. (2012). Ambient fabrication of flexible and large-area organic light-emitting devices using slot-die coating. Nat. Commun. *3*, 1002.

11. Zhao, W., Zhang, S., Zhang, Y., Li, S., Liu, X., He, C., Zheng, Z., and Hou, J. (2018). Environmentally friendly solvent-processed organic solar cells that are highly efficient and adaptable for the blade-coating method. Adv. Mater. *30*, 1704837.

12. Kang, Q., Yang, B., Xu, Y., Xu, B., and Hou, J. (2018). Printable MoO$_x$ anode interlayers for organic solar cells. Adv. Mater. *30*, 1801718.

13. He, Z.C., Zhong, C.M., Huang, X., Wong, W.Y., Wu, H.B., Chen, L.W., Su, S.J., and Cao, Y. (2011). Simultaneous enhancement of open-circuit voltage, short-circuit current density, and fill factor in polymer solar cells. Adv. Mater. *23*, 4636–4643.

14. Lv, M.L., Li, S.S., Jasieniak, J.J., Hou, J.H., Zhu, J., Tan, Z.A., Watkins, S.E., Li, Y.F., and Chen, X.W. (2013). A hyperbranched conjugated polymer as the cathode interlayer for high-performance polymer solar cells. Adv. Mater. *25*, 6889–6894.

15. Liu, S.J., Zhang, K., Lu, J.M., Zhang, J., Yip, H.L., Huang, F., and Cao, Y. (2013). High-efficiency polymer solar cells via the incorporation of an amino-functionalized conjugated metallopolymer as a cathode interlayer. J. Am. Chem. Soc. *135*, 15326–15329.

16. Lin, Y., Jin, Y., Dong, S., Zheng, W., Yang, J., Liu, A., Liu, F., Jiang, Y., Russell, T.P., Zhang, F., et al. (2018). Printed nonfullerene organic solar cells with the highest efficiency of 9.5%. Adv. Energy Mater. *8*, 1701942.

17. Gao, L., Zhang, Z.G., Xue, L., Min, J., Zhang, J., Wei, Z., and Li, Y. (2016). All-polymer solar cells based on absorption-complementary polymer donor and acceptor with high power conversion efficiency of 8.27%. Adv. Mater. *28*, 1884–1890.

18. Sun, D., Meng, D., Cai, Y., Fan, B., Li, Y., Jiang, W., Huo, L., Sun, Y., and Wang, Z. (2015). Non-fullerene-acceptor-based bulk-heterojunction organic solar cells with efficiency over 7. J. Am. Chem. Soc. *137*, 11156–11162.

19. Zhang, Z.-G., Qi, B., Jin, Z., Chi, D., Qi, Z., Li, Y., and Wang, J. (2014). Perylene diimides: a thickness-insensitive cathode interlayer for high performance polymer solar cells. Energy Environ. Sci. *7*, 1966–1973.

20. Liu, Y., Cole, M.D., Jiang, Y., Kim, P.Y., Nordlund, D., Emrick, T., and Russell, T.P. (2018). Chemical and morphological control of interfacial self-doping for efficient organic electronics. Adv. Mater. *30*, 1705976.

21. Zhao, K., Ye, L., Zhao, W., Zhang, S., Yao, H., Xu, B., Sun, M., and Hou, J. (2015). Enhanced efficiency of polymer photovoltaic cells via the incorporation of a water-soluble naphthalene diimide derivative as a cathode interlayer. J. Mater. Chem. C *3*, 9565–9571.

22. Jia, T., Sun, C., Xu, R., Chen, Z., Yin, Q., Jin, Y., Yip, H.L., Huang, F., and Cao, Y. (2017). Naphthalene diimide based n-type conjugated polymers as efficient cathode interfacial materials for polymer and perovskite solar cells. ACS Appl. Mater. Interfaces *9*, 36070–36081.

23. Hu, Z., Chen, Z., Zhang, K., Zheng, N., Xie, R., Liu, X., Yang, X., Huang, F., and Cao, Y. (2017). Self-doped n-type water/alcohol soluble-conjugated polymers with tailored backbones and polar groups for highly efficient polymer solar cells. Solar RRL *1*, 1700055.

24. Wu, Z., Sun, C., Dong, S., Jiang, X.-F., Wu, S., Wu, H., Yip, H.-L., Huang, F., and Cao, Y. (2016). n-Type water/alcohol-soluble naphthalene diimide-based conjugated polymers for high-performance polymer solar cells. J. Am. Chem. Soc. *138*, 2004–2013.

25. Guo, X., Wang, X., Zhang, J., Yu, S., Yu, W., Fu, P., Liu, X., Tu, D., and Li, C. (2018). Lowering molecular symmetry to improve morphological property of hole transport layer for stable perovskite solar cells. Angew. Chem. Int. Ed. https://doi.org/10.1002/anie.201807402.

26. Hawash, Z., Ono, L.K., Raga, S.R., Lee, M.V., and Qi, Y. (2015). Air-exposure induced dopant redistribution and energy level shifts in spin-coated Spiro-MeOTAD films. Chem. Mater. *27*, 562–569.

27. Kato, Y., Ono, L.K., Lee, M.V., Wang, S., Raga, S.R., and Qi, Y. (2015). Silver iodide formation in methyl ammonium lead iodide perovskite solar cells with silver top electrodes. Adv. Mater. Interfaces *2*, 1500195.

28. Ono, L.K., Raga, S.R., Remeika, M., Winchester, A.J., Gabe, A., and Qi, Y. (2015). Pinhole-free hole transport layers significantly improve the stability of MAPbI3-based perovskite solar cells under operating conditions. J. Mater. Chem. A *3*, 15451–15456.

29. Wang, Y., Yan, Z., Guo, H., Uddin, M.A., Ling, S., Zhou, X., Su, H., Dai, J., Woo, H.Y., and Guo, X. (2017). Effects of bithiophene imide fusion on the device performance of organic thin-film transistors and all-polymer solar cells. Angew. Chem. Int. Ed. *56*, 15304–15308.

30. Hou, J., Wu, Y., An, C., Shi, L., Yang, L., Qin, Y., Liang, N., He, C., and Wang, Z. (2018). Crucial role of chlorinated thiophene orientation in conjugated polymers for photovoltaic devices. Angew. Chem. Int. Ed. https://doi.org/10.1002/anie.201807865.

31. Jung, S.-K., Heo, J.H., Lee, D.W., Lee, S.-C., Lee, S.-H., Yoon, W., Yun, H., Im, S.H., Kim, J.H., and Kwon, O.P. (2018). Nonfullerene electron transporting material based on naphthalene diimide small molecule for highly stable perovskite solar cells with efficiency exceeding 20%. Adv. Funct. Mater. *28*, 1800346.

32. Huang, F., Wu, H., Wang, D., Yang, W., and Cao, Y. (2004). Novel electroluminescent conjugated polyelectrolytes based on polyfluorene. Chem. Mater. *16*, 708–716.

33. Sun, C., Wu, Z., Hu, Z., Xiao, J., Zhao, W., Li, H.-W., Li, Q.-Y., Tsang, S.-W., Xu, Y.-X., Zhang, K., et al. (2017). Interface design for high-efficiency non-fullerene polymer solar cells. Energy Environ. Sci. *10*, 1784–1791.

34. Zheng, D., Zhang, M., and Zhao, G. (2017). The promotion effects of thionation and isomerization on charge carrier mobility in naphthalene diimide crystals. Phys. Chem. Chem. Phys. *19*, 28175–28181.

35. Lee, W.-Y., Oh, J.H., Suraru, S.-L., Chen, W.-C., Würthner, F., and Bao, Z. (2011). High-mobility air-stable solution-shear-processed n-channel organic transistors based on core-chlorinated naphthalene diimides. Adv. Funct. Mater. *21*, 4173–4181.

36. Matsunaga, Y., Goto, K., Kubono, K., Sako, K., and Shinmyozu, T. (2014). Photoinduced color change and photomechanical effect of naphthalene diimides bearing alkylamine moieties in the solid state. Chem. Eur. J. *20*, 7309–7316.

37. Kao, C.-C., Lin, P., Shen, Y.-Y., Yan, J.-Y., Ho, J.-C., Lee, C.-C., and Chan, L.-H. (2008). Solid-state structure of the naphthalene-based n-type semiconductor, and performance improved with Mo-based source/drain electrodes. Synth. Met. *158*, 299–305.

38. Hexemer, A., Bras, W., Glossinger, J., Schaible, E., Gann, E., Kirian, R., MacDowell, A., Church, M., Rude, B., and Padmore, H. (2010). A SAXS/WAXS/GISAXS beamline with multilayer monochromator. J. Phys. Conf. Ser. *247*, 012007.

39. Smilgies, D.M., and Blasini, D.R. (2007). Indexation scheme for oriented molecular thin films studied with grazing-incidence reciprocal-space mapping. J. Appl. Cryst. *40*, 716–718.

40. Li, W., Ye, L., Li, S., Yao, H., Ade, H., and Hou, J. (2018). A high-efficiency organic solar cell enabled by the strong intramolecular electron push-pull effect of the nonfullerene acceptor. Adv. Mater. *30*, 1707170.

41. Xu, Q., Wang, F.Z., Tan, Z.A., Li, L.J., Li, S.S., Hou, X.L., Sun, G., Tu, X.H., Hou, J.H., and Li, Y.F. (2013). High-performance polymer solar cells with solution-processed and environmentally friendly CuO$_x$ anode buffer layer. ACS Appl. Mater. Interfaces *5*, 10658–10664.

42. Zhou, H., Zhang, Y., Seifter, J., Collins, S.D., Luo, C., Bazan, G.C., Nguyen, T.Q., and Heeger, A.J. (2013). High-efficiency polymer solar cells enhanced by solvent treatment. Adv. Mater. *25*, 1646–1652.

43. Zhao, W., Qian, D., Zhang, S., Li, S., Inganas, O., Gao, F., and Hou, J. (2016). Fullerene-free polymer solar cells with over 11% efficiency and excellent thermal stability. Adv. Mater. *28*, 4734–4739.

44. Li, S., Ye, L., Zhao, W., Zhang, S., Mukherjee, S., Ade, H., and Hou, J. (2016). Energy-level modulation of small-molecule electron acceptors to achieve over 12% efficiency in polymer solar cells. Adv. Mater. *28*, 9423–9429.

45. Zhang, H., Wang, X., Yang, L., Zhang, S., Zhang, Y., He, C., Ma, W., and Hou, J. (2017). Improved domain size and purity enables efficient all-

Please cite this article in press as: Kang et al., A Printable Organic Cathode Interlayer Enables over 13% Efficiency for 1-cm^2 Organic Solar Cells, Joule (2018), https://doi.org/10.1016/j.joule.2018.10.024

small-molecule ternary solar cells. Adv. Mater. *29*, 1703777.

46. Li, C.Z., Chueh, C.C., Ding, F.Z., Yip, H.L., Liang, P.W., Li, X.S., and Jen, A.K.Y. (2013). Doping of fullerenes via anion-induced electron transfer and its implication for surfactant facilitated high performance polymer solar cells. Adv. Mater. *25*, 4425–4430.

47. Chen, Z., Hu, Z., Wu, Z., Liu, X., Jin, Y., Xiao, M., Huang, F., and Cao, Y. (2017). Counterion-tunable n-type conjugated polyelectrolytes for the interface engineering of efficient polymer solar cells. J. Mater. Chem. A *5*, 19447–19455.

48. Smith, C., Rhodes, R., Beliatis, M., Jayawardena, K., Rozanski, L., Mills, C., and Silva, S. (2014). Graphene oxide hole transport layers for large area, high efficiency organic solar cells. Appl. Phys. Lett. *105*, 073304.

49. Cui, C., Guo, X., Min, J., Guo, B., Cheng, X., Zhang, M., Brabec, C., and Li, Y. (2015). High-performance organic solar cells based on a small molecule with alkylthio-thienyl-conjugated side chains without extra treatments. Adv. Mater. *27*, 7469–7475.

50. Ye, F., Chen, Z., Zhao, X., Chen, J., and Yang, X. (2015). "Layer-filter threshold" technique for near-infrared laser ablation in organic semiconductor device processing. Adv. Energy Mater. *25*, 4453–4461.

51. Guo, B., Li, W., Guo, X., Meng, X., Ma, W., Zhang, M., and Li, Y. (2017). High efficiency nonfullerene polymer solar cells with thick active layer and large area. Adv. Mater. *29*, 1702291.

JOUL, Volume *3*

Supplemental Information

A Printable Organic Cathode Interlayer Enables over 13% Efficiency for 1-cm^2 Organic Solar Cells

Qian Kang, Long Ye, Bowei Xu, Cunbin An, Samuel J. Stuard, Shaoqing Zhang, Huifeng Yao, Harald Ade, and Jianhui Hou

Joule

CellPress

Supporting Information

Contents

Supplemental Figures

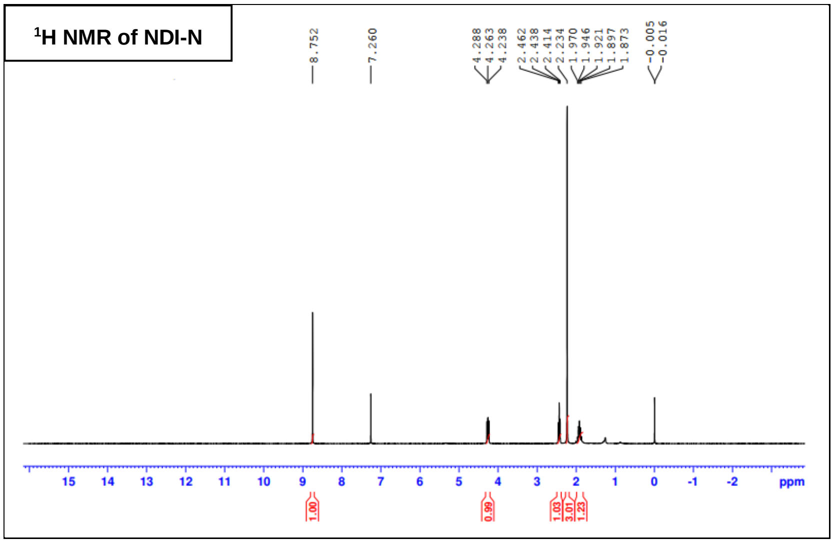

^{1}H NMR of NDI-N

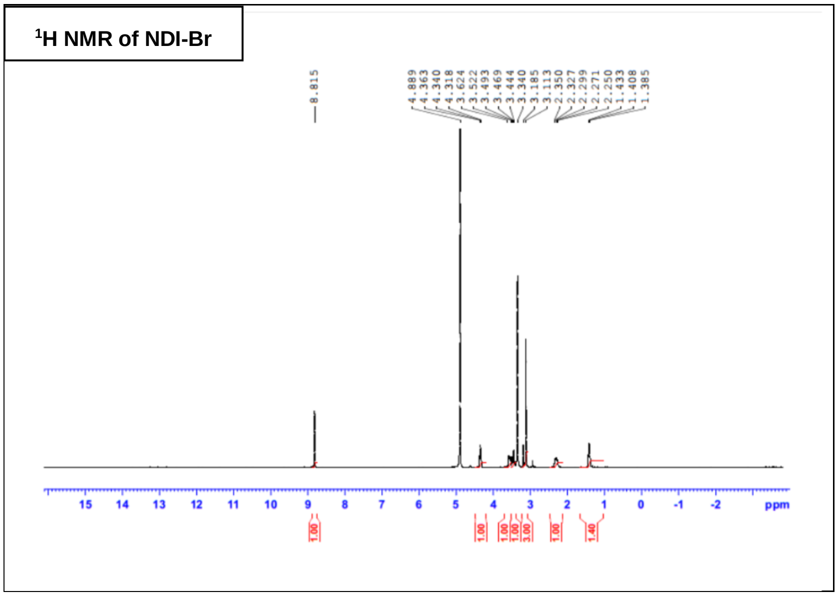

^{1}H NMR of NDI-Br

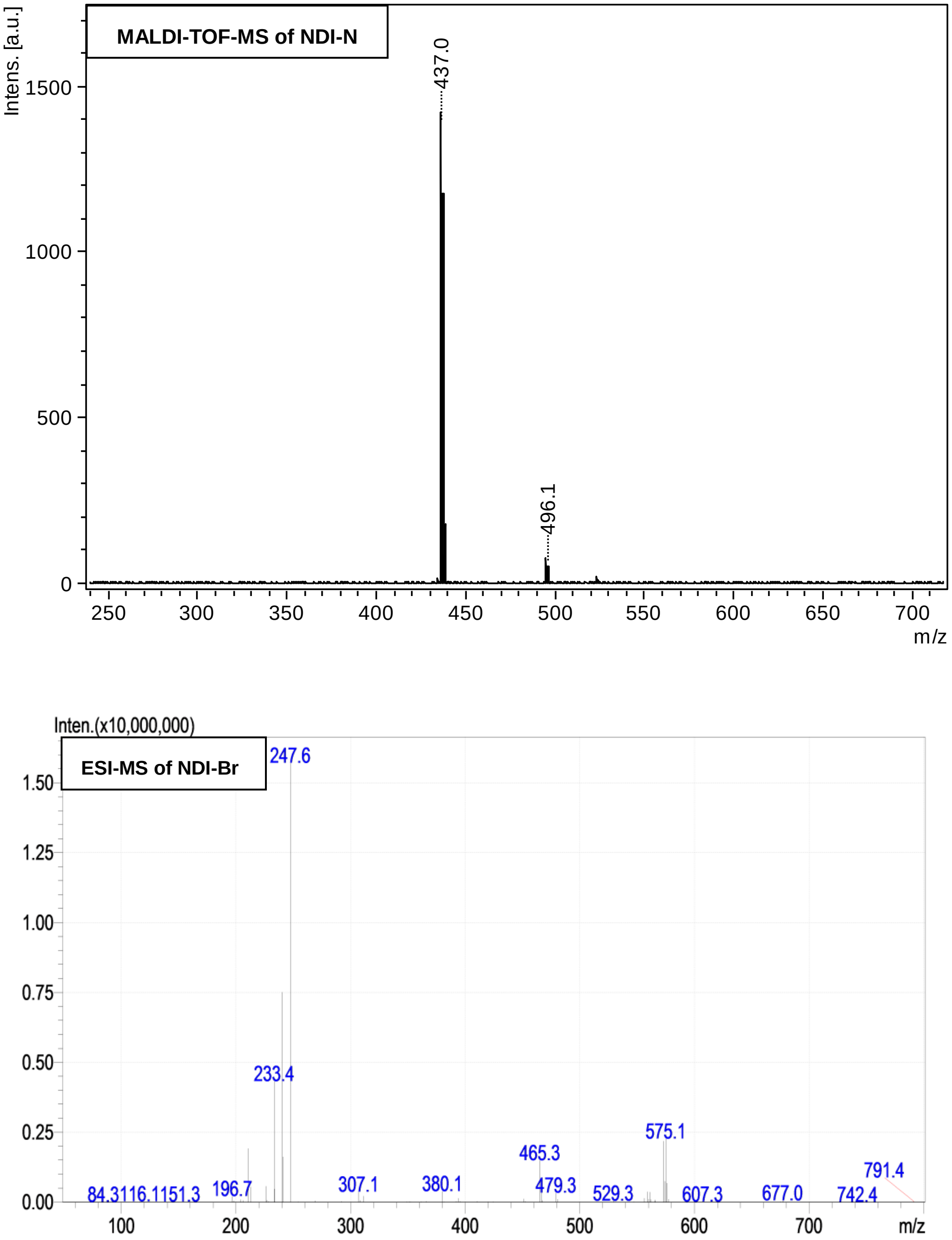

Figure S1. ^{1}H NMR and MALDI-TOF-MS of NDI-N (solvent: $CDCl_3$); ^{1}H NMR and ESI-MS of NDI-Br (solvent: CD_3OD).

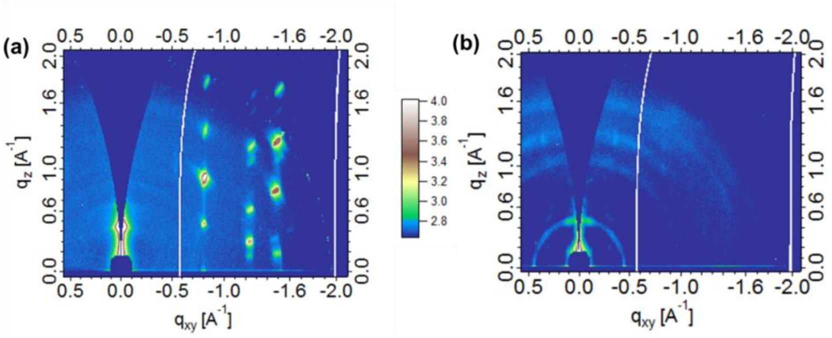

Figure S2. 2D GIWAXS patterns of (a) NDI-N and (b) NDI-Br neat film on Si.

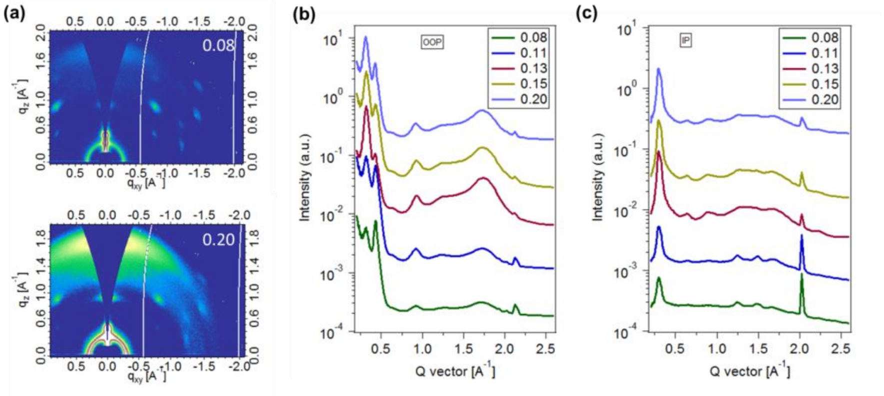

Figure S3. (a) 2D GIWAXS patterns of NDI-N film using 0.08º and 0.20º degrees incident angles; (b) Out-of-plane and (c) In-plane line-profiles as a function of incident angles.

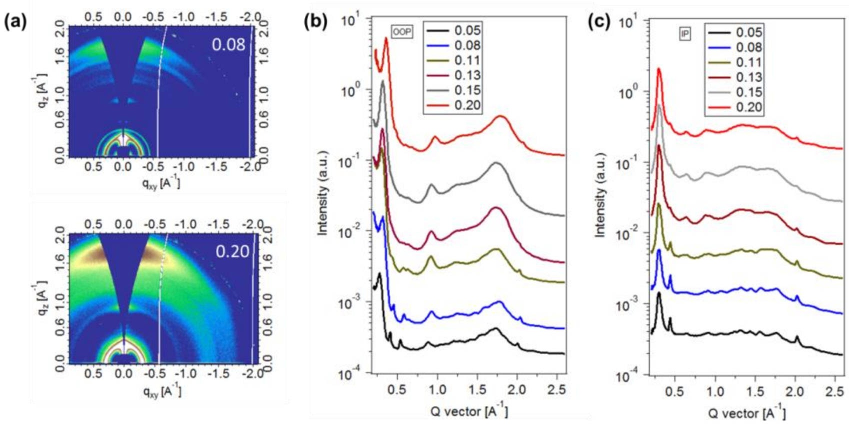

Figure S4. (a) 2D GIWAXS patterns of NDI-Br film using 0.08º and 0.20º incident angles; (b) Out-of-plane and (c) In-plane line-profiles as a function of incident angles.

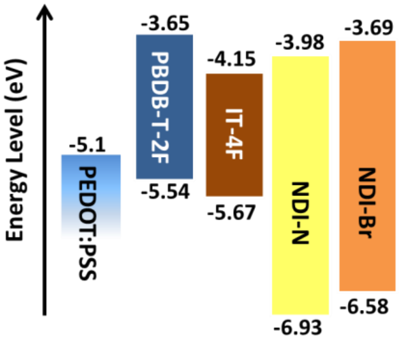

Figure S5. Schematic energy-level diagrams of PEDOT:PSS, PBDB-T-2F, IT-4F, NDI-N, and NDI-Br.

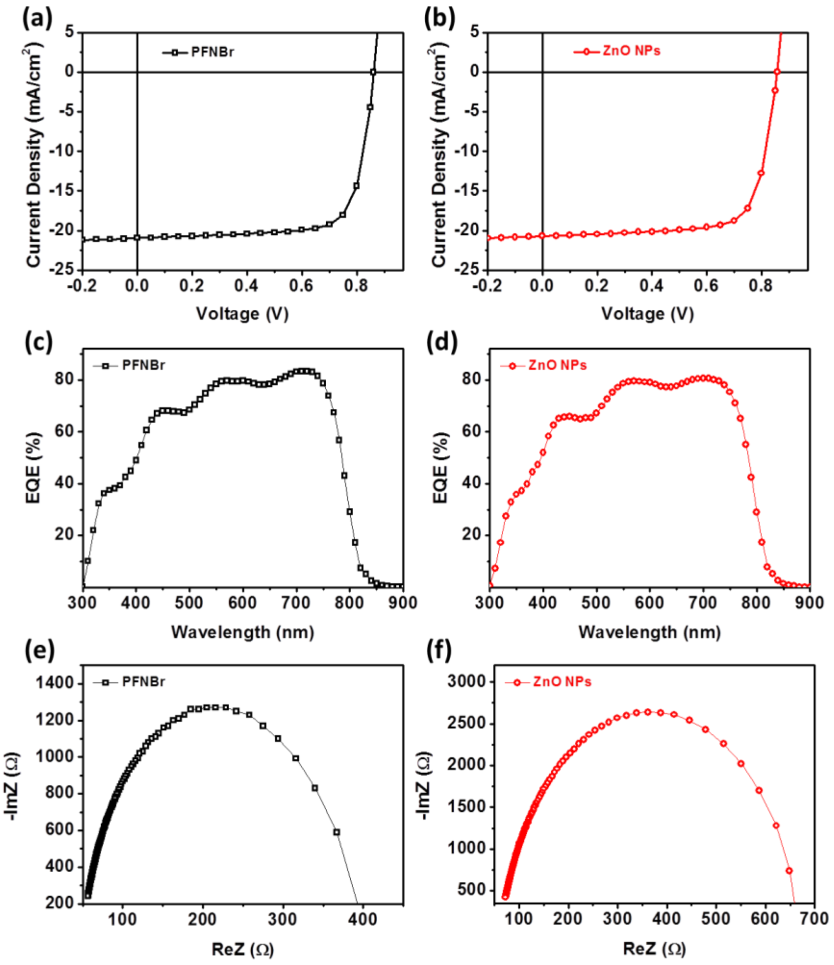

Figure S6. (a and b) *J-V*, (c and d) EQE curves of devices with PFN-Br and ZnO NPs CILs. (e and f) Nyquist plots of devices with PFN-Br and ZnO NPs CILs.

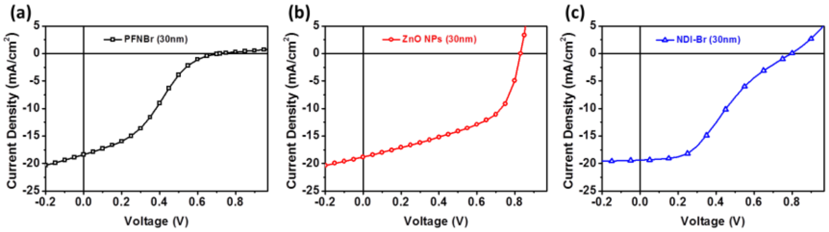

Figure S7. *J-V* characteristics of devices with (a) PFN-Br, (b) ZnO NPs and (c) NDI-Br at the thickness of 30 nm.

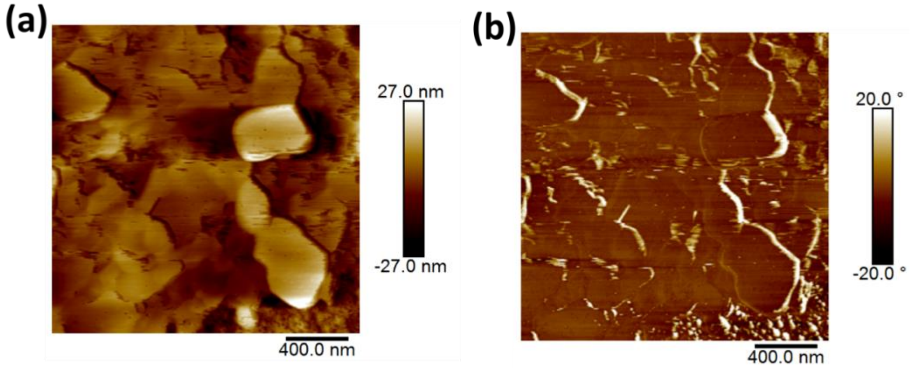

Figure S8. Tapping-mode AFM (a) height and (b) phase images of NDI-N film on the ITO substrate.

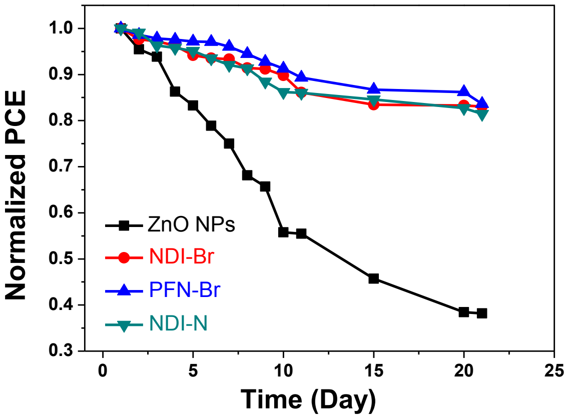

Figure S9. Normalized PCE values as a function of exposure time under ambient conditions for devices with ZnO NPs, NDI-N, PFN-Br, and NDI-Br CILs.

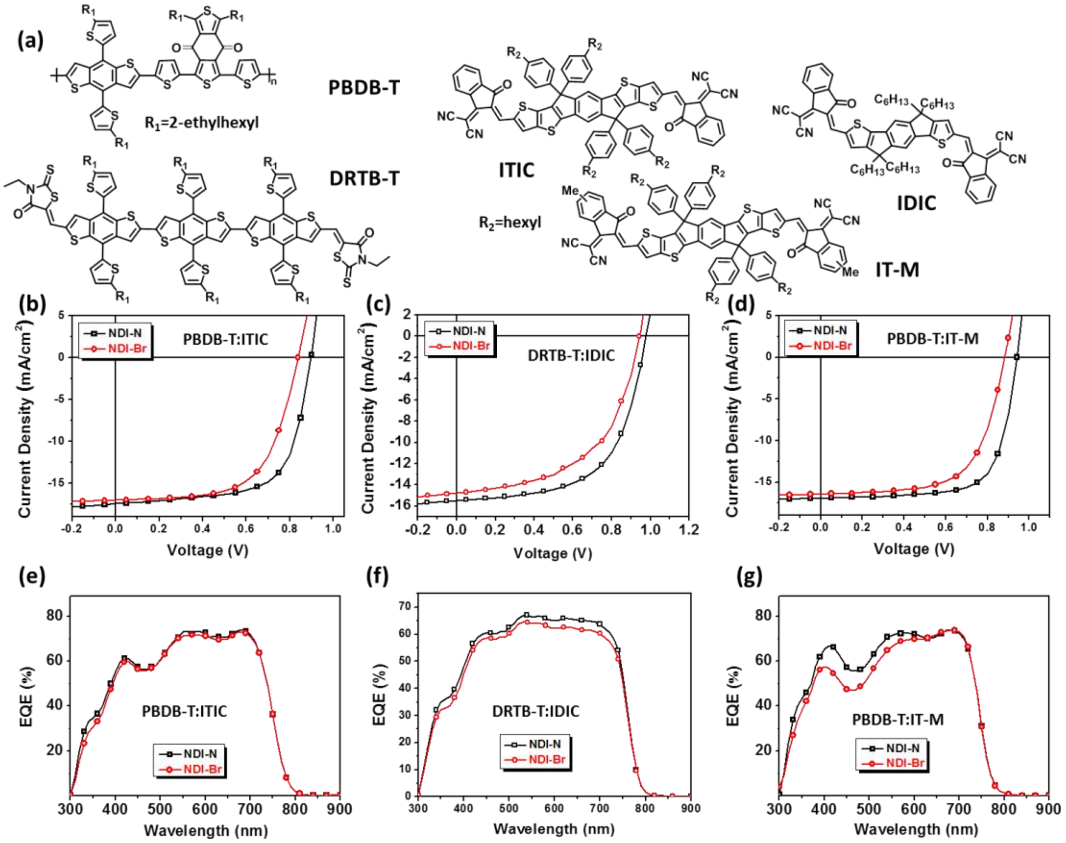

Figure S10. (a) Chemical structures of PBDB-T, DRTB-T, ITIC, IDIC, IT-M. (b), (c), (d) *J-V* and (e), (f), (g) EQE curves of the NDI-N and NDI-Br films with different active layers.

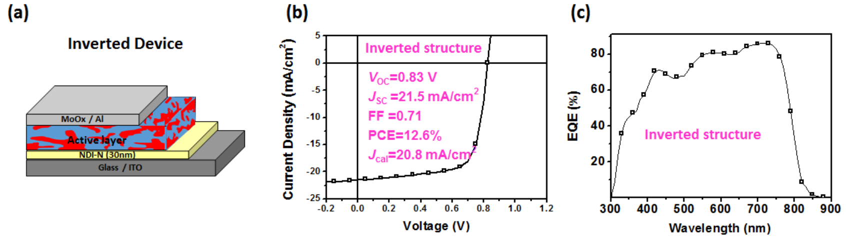

Figure S11. (a) Devices structure of the inverted structure based on NDI-N films. (b) *J-V* and (c) EQE curves of the devices based on NDI-N film.

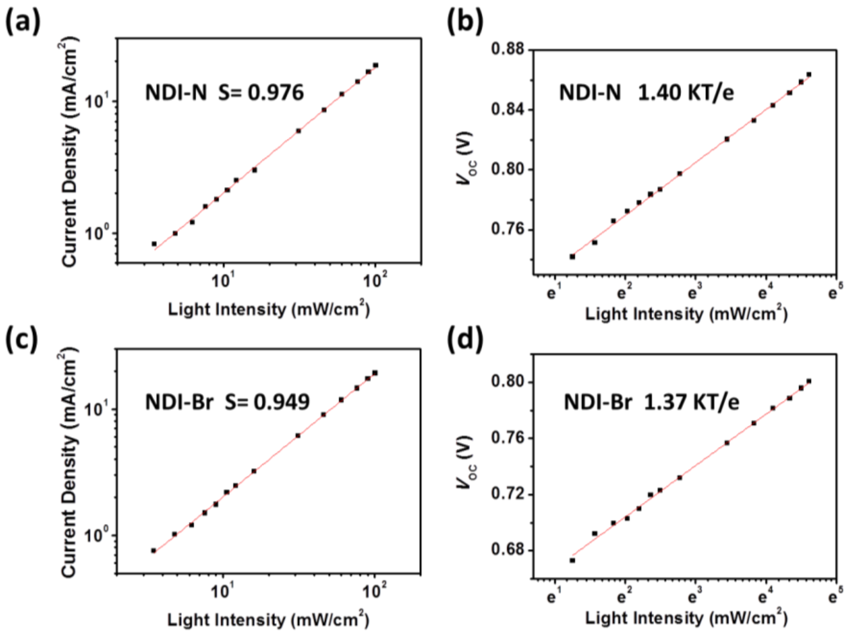

Figure S12. (a) Dependence of the short-circuit current density and (b) the open-circuit voltage of NDI-N-modified devices on light intensity. (c) Dependence of the short-circuit current density and (d) the open-circuit voltage of NDI-Br-modified devices on light intensity.

Figure S12 shows the dependence of the J_{sc} of the studied devices modified with NDI-N and NDI-Br on the light intensity (P_{light}). The relationship between J_{sc} and P_{light} can be expressed by the power-law equation $J_{sc} \propto P_{light}^{\alpha}$, where α is the power-law exponent. The α values were determined to be 0.976 and 0.949 for the OSCs modified with NDI-N and NDI-Br, respectively, meaning that bimolecular recombination was greatly suppressed in these NDI-modified devices.

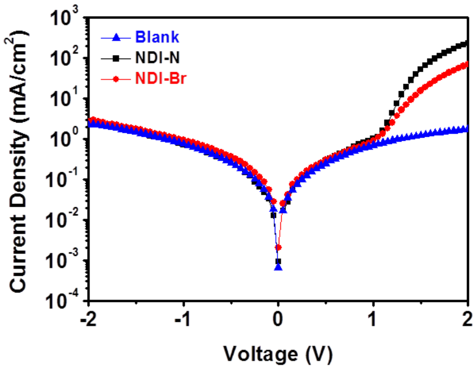

Figure S13. Current density-voltage (J-V) characteristics of the PSC devices based on blank, NDI-N and NDI-Br in dark.

The effect of n-doping of the non-fullerene acceptor on the rectification characteristic of fullerene-free devices was also investigated by fabricating p-n junction diodes with a structure of ITO/PEDOT:PSS/IT-4F/NDI-based compound (20 nm)/Al and measuring the J-V characteristics in the dark. Here, PEDOT: PSS is used as the p-type semiconductor and the bilayer film of IT-4F/NDI-based compound acts as the n-type semiconductor for constructing the p-n junction. As shown in Figure S13, the rectification ratio (the quotient of the current density at ±2 V) of the NDI-N-based diode is three times higher than that of the NDI-Br-based device, suggesting that the rectification characteristic of OSC devices can be effectively enhanced by doping the non-fullerene acceptor.

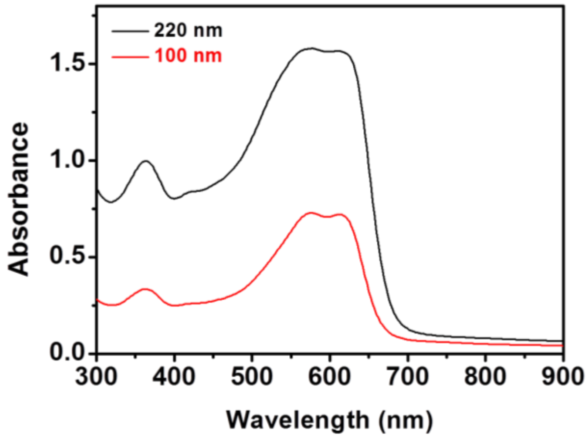

Figure S14. UV-vis absorption spectra of the films with 100nm and 220nm of PBDB-T-2F.

Considering that the thickness of PBDB-T-2F (220 nm) used in the bilayer device is much thicker than that of the active layer (100 nm) in bulk heterojunction (BHJ) OSCs, the light-harvesting at the PBDB-T-2F/NDI-N interface is significantly depressed due to the strong absorption of the 220 nm PBDB-T-2F layer (Figure S14), and therefore, the real J_{sc} enhancement might be more pronounced in the NDI-N-modified BHJ devices.

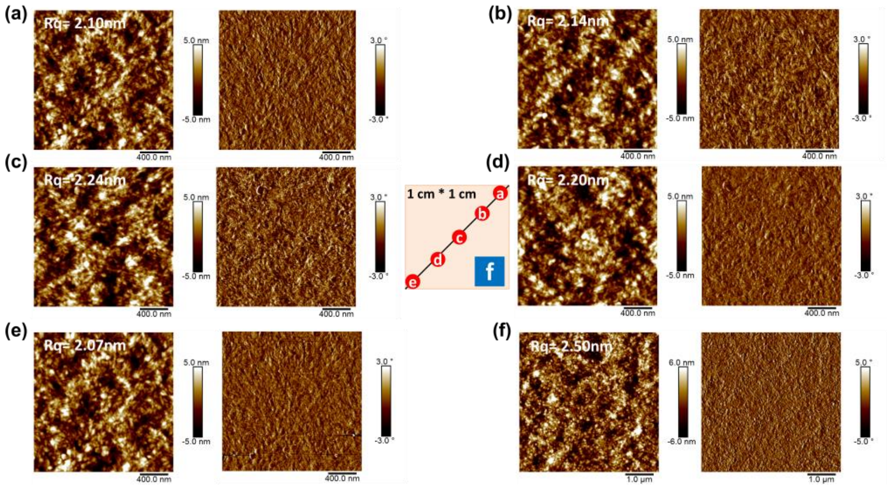

Figure S15. (a)-(e) 2 µm× 2 µm AFM images of five different spots collected along the diagonal line of a 1cm^2 NDI-N film and (f) 5 µm× 5 µm AFM height and phase images of NDI-N film.

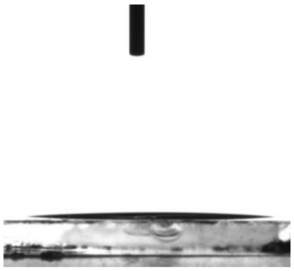

Figure S16. Contact angle of the CIL methanol solution drop on the PBDB-T-2F:IT-4F surface.

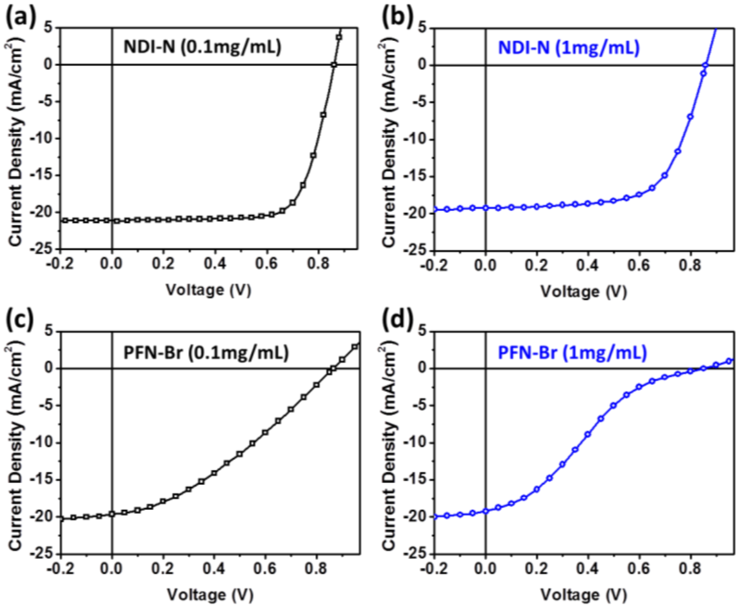

Figure S17. *J-V* curves of (a) (c) relatively thinner and (b) (d) thicker CILs with blade coated devices.

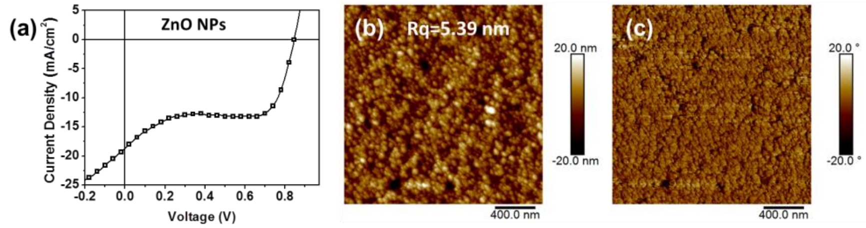

Figure S18. (a) *J-V* curves of blade-coating ZnO NPs-based device and (b) (c) AFM of ZnO NPs.

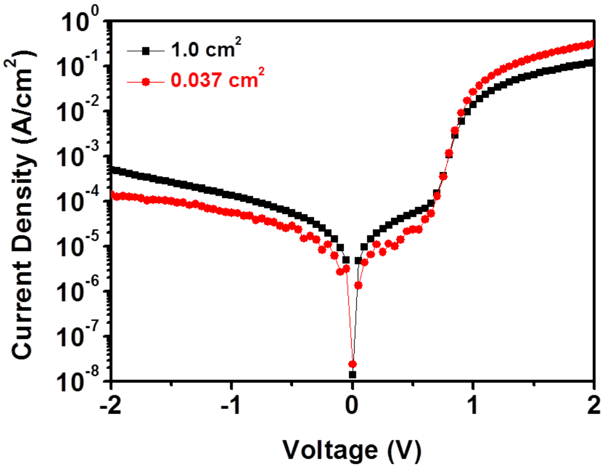

Figure S19. *J-V* characteristic of the large-area device and the normal-area device under dark.

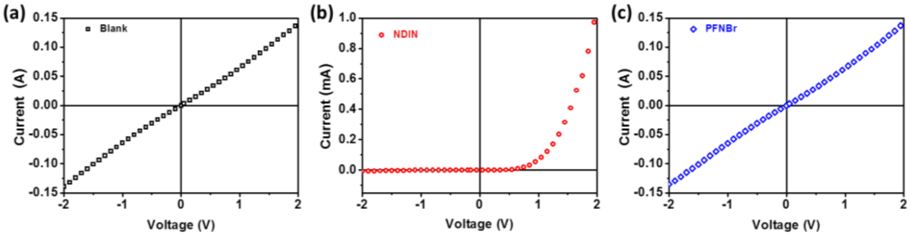

Figure S20. *J-V* characteristics of devices with the structures of (a) ITO/PEDOT:PSS/Al, (b) ITO/PEDOT:PSS/NDI-N/Al and (c) ITO/PEDOT:PSS/PFN-Br/Al.

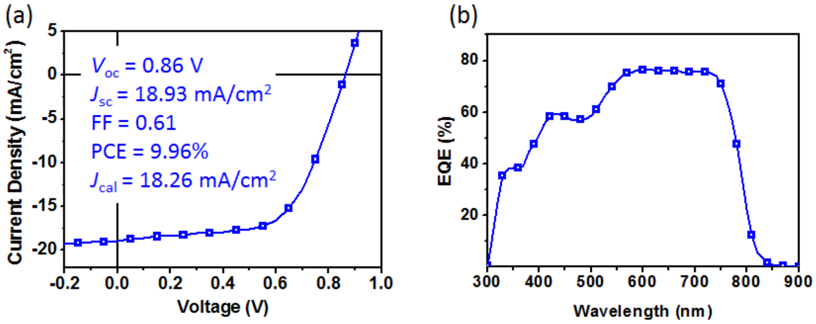

Figure S21. (a) *J-V* and (b) EQE curves of 1.0 cm^2 all-printed OSC.

To demonstrate the use of NDI-N in making all-printed OSCs, all-printed device of 1.0 cm^2 was fabricated through the blade-coating method. The fabrication of all-printed device was provided in Section 2 (Device fabrication). The all-printed OSC device exhibited a PCE of 9.96%, along with a J_{sc} of 18.93 mA/cm^2, a V_{oc} of 0.86 V, and an FF of 0.61. The calculated J_{sc} value from the EQE curves were 18.26 mA/cm^2 for the device, which agreed well with the J_{sc} value obtained from the *J-V* curves.

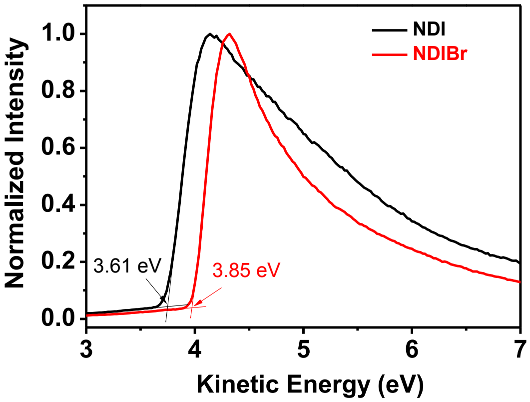

Figure S22. UPS spectra of NDI-N and NDI-Br.

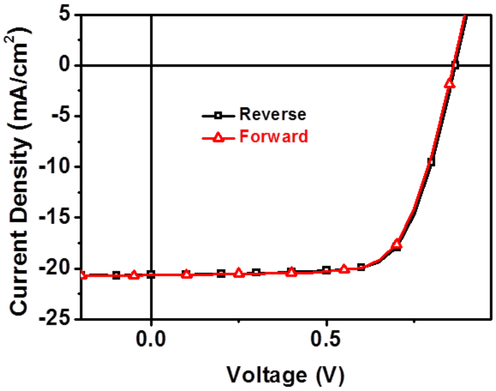

Figure S23. *J-V* curves of 1.0 cm^2 device at different scanning directions.

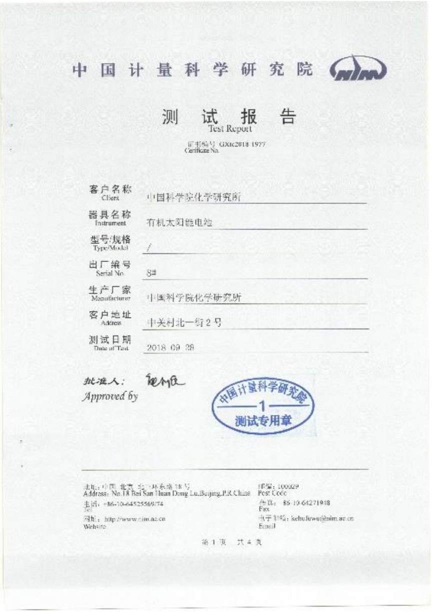

中国计量科学研究院

测 试 报 告
Test Report

证书编号 GXtc2018-1977
Certificate No.

客户名称 Client　中国科学院化学研究所
器具名称 Instrument　有机太阳能电池
型号/规格 Type/Model　/
出厂编号 Serial No.　8#
生产厂家 Manufacturer　中国科学院化学研究所
客户地址 Address　中关村北一街2号
测试日期 Date of Test　2018 09 28

批准人：
Approved by

地址：中国 北京 北三环东路18号
Address: No.18 Bei San Huan Dong Lu,Beijing,P.R.China
邮编：100029
Post Code
电话：+86-10-64525569/74
Tel
传真：86-10-64271948
Fax
网址：http://www.nim.ac.cn
Website
电子邮箱：kehufuwu@nim.ac.cn
Email

第 1 页　共 4 页

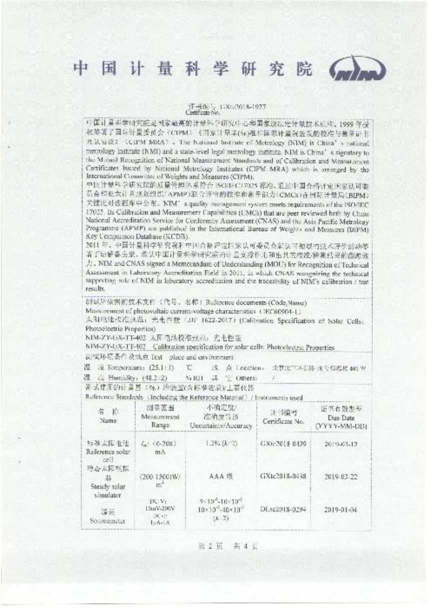

中国计量科学研究院

证书编号 GXtc2018-1977
Certificate No.

中国计量科学研究院是国家最高的计量科学研究中心和国家级法定计量技术机构。1999 年受权签署了国际计量委员会（CIPM）《国家计量基(标)准和国家计量院签发的校准与测量证书互认协议》（CIPM MRA）。The National Institute of Metrology (NIM) is China' s national metrology institute (NMI) and a state-level legal metrology institute. NIM is China' s signatory to the Mutual Recognition of National Measurement Standards and of Calibration and Measurement Certificates Issued by National Metrology Institutes (CIPM MRA) which is arranged by the International Committee of Weights and Measures (CIPM).

中国计量科学研究院的质量管理体系符合 ISO/IEC17025 标准，通过中国合格评定国家认可委员会和亚太计量规划组织（APMP）联合评审的校准和测量能力（CMCs）在国际计量局（BIPM）关键比对数据库中公布。NIM' s quality management system meets requirements of the ISO/IEC 17025. Its Calibration and Measurement Capabilities (CMCs) that are peer reviewed both by China National Accreditation Service for Conformity Assessment (CNAS) and the Asia Pacific Metrology Programme (APMP) are published in the International Bureau of Weights and Measures (BIPM) Key Comparison Database (KCDB).

2011 年，中国计量科学研究院和中国合格评定国家认可委员会就认可领域的技术评价活动签署了谅解备忘录，承认中国计量科学研究院的计量支撑作用和出具的校准/检测结果的溯源效力。NIM and CNAS signed a Memorandum of Understanding (MOU) for Recognition of Technical Assessment in Laboratory Accreditation Field in 2011, in which CNAS recognizing the technical supporting role of NIM in laboratory accreditation and the traceability of NIM's calibration / test results.

测试所依据的技术文件（代号，名称）Reference documents (Code,Name)
Measurement of photovoltaic current-voltage characteristics（IEC60904-1）
太阳电池校准规范：光电性能（JJF 1622-2017）(Calibration Specification of Solar Cells: Photoelectric Properties)
NIM-ZY-GX-TT-402 太阳电池校准规范：光电性能
NIM-ZY-GX-TT-402 Calibration specification for solar cells: Photoelectric Properties

测试环境条件及地点 Test place and environment
温 度 Temperature：(25.1±1) ℃　地 点 Location：北京北三环东路 18 号[illegible] 401 室
湿 度 Humidity：(48.2±2) %RH　其 它 Others：/

测试使用的计量基（标）准装置(含标准物质)/主要仪器
Reference Standards（Including the Reference Material）/ Instruments used

名 称 Name	测量范围 Measurement Range	不确定度/准确度等级 Uncertainty/Accuracy	证书编号 Certificate No.	证书有效期至 Due Date (YYYY-MM-DD)
标准太阳电池 Reference solar cell	I_{sc}:（0-200）mA	1.2% (k=2)	GXtc2018-0439	2019-03-12
稳态太阳模拟器 Steady solar simulator	(200-1500)W/m^2	AAA 级	GXtc2018-0438	2019-03-22
源表 Sourcemeter	DC V: 10mV-200V DC I: 1μA-1A	5×10^{-6}-10×10^{-5} 10×10^{-5}-40×10^{-5} (k=2)	DLsc2018-0294	2019-01-04

第 2 页　共 4 页

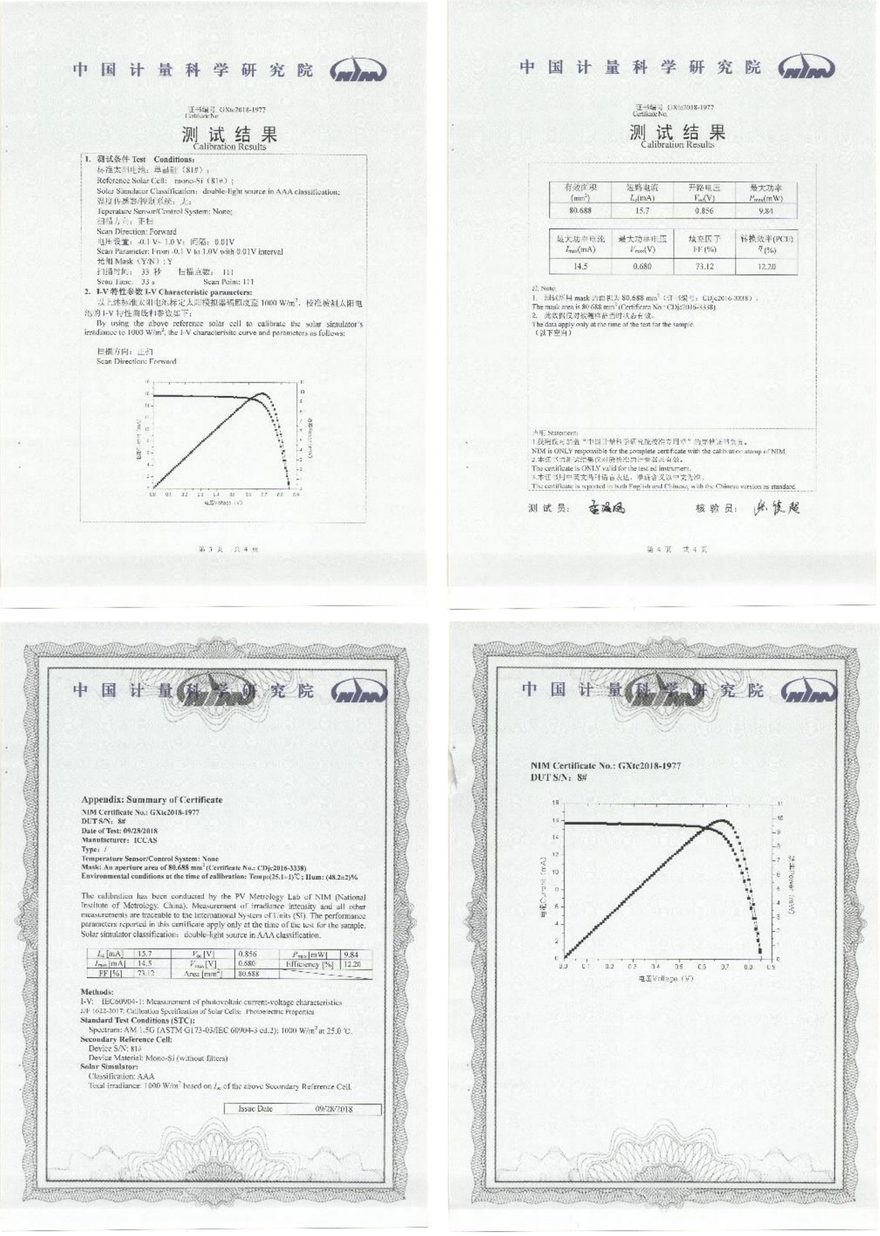

中国计量科学研究院

证书编号 GXtc2018-1977
Certificate No.

测试结果
Calibration Results

1. **测试条件 Test Conditions:**
标准太阳电池：单晶硅（81#）；
Reference Solar Cell: mono-Si（81#）；
Solar Simulator Classification: double-light source in AAA classification;
温度传感器/控制系统：无；
Teperature Sensor/Control System: None;
扫描方向：正扫
Scan Direction: Forward
电压设置：-0.1 V~1.0 V；间隔：0.01V
Scan Parameter: From -0.1 V to 1.0V with 0.01V interval
光阑 Mask（Y/N）：Y
扫描时间： 33 秒 扫描点数： 111
Scan Time: 33 s Scan Point: 111

2. **I-V 特性参数 I-V Characteristic parameters:**

以上述标准太阳电池标定太阳模拟器辐照度至 1000 W/m²，校准被测太阳电池的 I-V 特性曲线和参数如下：

By using the above reference solar cell to calibrate the solar simulator's irradiance to 1000 W/m², the I-V characterisite curve and parameters as follows:

扫描方向：正扫
Scan Direction: Forward

第 3 页 共 4 页

中国计量科学研究院

证书编号 GXtc2018-1977
Certificate No.

测试结果
Calibration Results

有效面积 (mm²)	短路电流 I_{sc}(mA)	开路电压 V_{oc}(V)	最大功率 P_{max}(mW)
80.688	15.7	0.856	9.84

最大功率电流 I_{max}(mA)	最大功率电压 V_{max}(V)	填充因子 FF (%)	转换效率(PCE) η (%)
14.5	0.680	73.12	12.20

注 Note:
1. 测试所用 mask 的面积为 80.688 mm²（证书编号：CDjc2016-3338）。
The mask area is 80.688 mm² (Certificate No.: CDjc2016-3338).
2. 此数据仅对被测样品当时状态有效。
The data apply only at the rime of the test for the sample.
（以下空白）

声明 Statement:
1.我院仅对加盖"中国计量科学研究院校准专用章"的完整证书负责。
NIM is ONLY responsible for the complete certificate with the calibration stamp of NIM.
2.本证书的测试结果仅对所校准的计量器具有效。
The certificate is ONLY valid for the test ed instrument.
3.本证书用中英文两种语言表达，准确含义以中文为准。
The certificate is reported in both English and Chinese, with the Chinese version as standard.

测试员：　　　核验员：

第 4 页 共 4 页

中国计量科学研究院

Appendix: Summary of Certificate

NIM Certificate No.: GXtc2018-1977
DUT S/N：8#
Date of Test: 09/28/2018
Manufacturer：ICCAS
Type：/
Temperature Sensor/Control System: None
Mask: An aperture area of 80.688 mm² (Certificate No.: CDjc2016-3338)
Environmental conditions at the time of calibration: Temp:(25.1±1)℃; Hum: (48.2±2)%

The calibration has been conducted by the PV Metrology Lab of NIM (National Institute of Metrology, China). Measurement of irradiance intensity and all other measurements are traceable to the International System of Units (SI). The performance parameters reported in this certificate apply only at the time of the test for the sample. Solar simulator classification：double-light source in AAA classification.

I_{sc} [mA]	15.7	V_{oc} [V]	0.856	P_{max} [mW]	9.84
I_{max} [mA]	14.5	V_{max} [V]	0.680	Efficiency [%]	12.20
FF [%]	73.12	Area [mm²]	80.688		

Methods:
I-V: IEC60904-1: Measurement of photovoltaic current-voltage characteristics
JJF 1622-2017: Calibration Specification of Solar Cells: Photoelectric Properties
Standard Test Conditions (STC):
Spectrum: AM 1.5G (ASTM G173-03/IEC 60904-3 ed.2); 1000 W/m² at 25.0 ℃.
Secondary Reference Cell:
Device S/N: 81#
Device Material: Mono-Si (without filters)
Solar Simulator:
Classification: AAA
Total irradiance: 1000 W/m² based on I_{sc} of the above Secondary Reference Cell.

Issue Date	09/28/2018

中国计量科学研究院

NIM Certificate No.: GXtc2018-1977
DUT S/N：8#

Figure S24. Certification report of 0.81 cm² (0.9 cm×0.9 cm mask) device from National Institute of Metrology (NIM).

Supplemental Tables

Table S1. Elemental analysis results.

NDI-N	**Calculation value**	**Analysis value**
N	12.83%	12.82%
C	66.04%	66.05%
H	6.47%	6.60%
NDI-Br	**Calculation value**	**Analysis value**
N	8.56%	8.40%
C	51.39%	49.61%
H	5.85%	5.98%
Br	24.42%	24.16%

Table S2. Photovoltaic parameters of devices based on NDI-N films with different thicknesses.

Thickness of NDI-N (nm)	**V_{oc} (V)**	**J_{sc} (mA/cm^2)**	**FF**	**PCE (%)**
5	0.86	20.8	0.76	13.5
8	0.86	21.1	0.76	13.7
10	0.86	21.3	0.76	13.9
15	0.86	19.4	0.74	12.4
30	0.86	18.1	0.75	11.6
40	0.85	16.3	0.74	10.5
50	0.86	15.9	0.74	10.2

Table S3. Photovoltaic parameters of devices based on different thicknesses of NDI-Br; 30nm of PFNBr and ZnO NPs.

Thickness of NDI-Br (nm)	V_{oc} (V)	J_{sc} (mA/cm^2)	FF	PCE (%)
10	0.80	20.1	0.71	11.5
15	0.80	19.2	0.52	8.21
30	0.80	19.4	0.34	5.20
40	0.75	9.56	0.11	0.78
PFN-Br (30nm)	0.72	18.4	0.31	4.08
ZnO NPs (30nm)	0.83	18.8	0.50	7.88

Table S4. The fitting results of the Nyquist plots of different CIL-modified devices.

CIL	Rsurface (Ω)
Methyl	6475
NDI-N	586.6
NDI-Br	884.2
PFN-Br	359.3
ZnO NPs	751.8

Table S5. Photovoltaic parameters of devices based on NDI-N films in inverted structure with different annealing temperature.

Temperature (°C)	V_{oc} (V)	J_{sc} (mA/cm^2)	FF	PCE (%)

0	0.77	17.4	0.58	7.71
100	0.80	20.7	0.64	10.6
130	0.83	21.1	0.68	11.9
150	0.83	21.5	0.71	12.6
200	0.68	19.1	0.62	8.07

Table S6. Photovoltaic parameters based on the bilayer heterojunction devices of ITO/PEDOT: PSS/PBDB-T-2F/NDI-based compound/PFN-Br/Al.

Devices	V_{oc} (V)	J_{sc} (mA/cm^2)	FF	PCE (%)
Blank	1.26	0.034	0.33	0.01
NDI-N	1.25	0.225	0.36	0.10
NDI-Br	1.27	0.068	0.31	0.03

Table S7. Crystal data.

Molecular formula	$C_{24}H_{28}N_4O_4$	
Molecular weight	436.50	
Temperature	173.15 K	
Wavelength	0.71073 Å	
Crystal system	Triclinic	
Space group	P-1	
Unit cell dimensions	a = 4.977(3) Å	α= 86.845(15)°.
	b = 7.685(5) Å	β= 83.40(2)°.
	c = 14.369(8) Å	γ = 89.63(2)°.
Volume	545.2(5) Å^3	
Z	1	
Density (calculated)	1.330 Mg/m^3	
Absorption coefficient	0.092 mm^{-1}	
F(000)	232	
Crystal size	0.513 x 0.434 x 0.039 mm^3	
Theta range for data collection	2.654 to 27.468°.	
Index ranges	-6<=h<=6, -9<=k<=9, -18<=l<=18	
Reflections collected	9306	
Independent reflections	2483 [R(int) = 0.0556]	
Completeness to theta = 25.242°	99.5 %	
Absorption correction	Semi-empirical from equivalents	
Max. and min. transmission	1.00000 and 0.76614	
Refinement method	Full-matrix least-squares on F^2	
Data / restraints / parameters	2483 / 2 / 177	

Goodness-of-fit on F^2	1.158
Final R indices [I>2sigma(I)]	R1 = 0.0685, wR2 = 0.1658
R indices (all data)	R1 = 0.0754, wR2 = 0.1713
Extinction coefficient	n/a
Largest diff. peak and hole	0.278 and -0.225 e.$Å^{-3}$

Table S8. Atomic coordinates (x 10^4) and equivalent isotropic displacement parameters ($Å^2$x 10^3)

	x	y	z	U(eq)
O1	-536(3)	1447(2)	7249(1)	41(1)
N1	2994(3)	3162(2)	6624(1)	29(1)
C1	1450(3)	1643(2)	6678(1)	30(1)
N2	2671(5)	7377(3)	8506(2)	43(1)
C2	2337(3)	305(2)	5999(1)	26(1)
O2	6608(2)	4839(2)	6037(1)	36(1)
C3	4609(3)	628(2)	5333(1)	24(1)
C4	6124(3)	2179(2)	5310(1)	26(1)
C5	5320(3)	3500(2)	6006(1)	28(1)
C6	901(3)	-1222(2)	6008(1)	30(1)
C7	8329(3)	2468(2)	4652(1)	29(1)
C8	2134(4)	4496(2)	7300(1)	33(1)
C9	3436(4)	4214(3)	8201(1)	41(1)
C10	2472(5)	5552(3)	8910(1)	46(1)
C11	1649(8)	8577(5)	9221(3)	70(1)
C12	5434(15)	7831(11)	8160(5)	81(3)
N2A	4309(14)	6946(9)	9004(5)	37(2)
C11A	3120(20)	8014(15)	9777(7)	53(3)
C12A	4690(50)	7980(30)	8113(9)	48(5)

Table S9. The PCEs (%) of 30 cells for 1.0 cm^2.

No.1	**No.2**	**No.3**	**No.4**	**No.5**	**No.6**	**No.7**	**No.8**	**No.9**	**No.10**
11.39	11.40	11.46	11.65	11.79	11.79	11.82	11.91	11.92	11.96
No.11	**No.12**	**No.13**	**No.14**	**No.15**	**No.16**	**No.17**	**No.18**	**No.19**	**No.20**
11.99	12.00	12.12	12.12	12.18	12.26	12.34	12.49	12.51	12.51
No.21	**No.22**	**No.23**	**No.24**	**No.25**	**No.26**	**No.27**	**No.28**	**No.29**	**No.30**
12.54	12.63	12.66	12.74	12.80	12.87	12.94	12.98	13.10	13.15

Table S10. Photovoltaic parameters of devices based on different CILs with different thicknesses by blade-coating.

Devices	V_{oc} (V)	J_{sc} (mA/cm^2)	FF	PCE (%)
NDI-N (0.1mg/mL)	0.86	21.1	0.72	13.2
NDI-N (1mg/mL)	0.86	19.3	0.65	10.8
PFN-Br (0.1mg/mL)	0.87	19.7	0.34	5.76
PFN-Br (1mg/mL)	0.85	20.2	0.24	4.09
ZnO NPs	0.85	18.7	0.56	8.89

Experimental Procedures

1. Materials

Polymer PBDB-T-2F and IT-4F were purchased from Solarmer Materials Inc. PEDOT:PSS, Clevios^{TM} P VP AI 4083, was commercially available from Heraeus. The other material and solvent were common commercial level and used as received.

Synthesis

1) **(*N*,*N*-dimethylamino)propyl naphthalimide (NDI-N)** NDI-N was synthesized according to the reported procedures. ^{1}H NMR (400 MHz, CDCl$_3$, δ_{ppm}): 8.75(s, 4H), 4.26(t, 4H), 2.43(t, 4H), 2.23(s, 12H), 1.92(m, 4H); Anal. Calcd for [$C_{28}H_{38}Br_2N_4O_4$]: C, 66.04; H, 6.47; Found: C, 66.05; H, 6.60; MALDI-TOF (*m*/*z*): 436.21; Found: 437.0.

(*N*,*N*-dimethyl)-*N*-ethylammonium)propyl naphthalimide (NDI-Br) A 100-mL flask with a magnetic stirring bar was charged with NDI-N (200 mg) dissolved in 40 mL of THF. To this solution was added bromoethane (2 g, 18 mmol) and 10 mL of DMSO. The reaction mixture was stirred at 50°C for 3 days. THF and extra bromoethane were removed by reduced pressure distillation. Afterwards, NDI-Br was purified by recrystallization in ethanol with a yield of 72%. ^{1}H NMR (400 MHz, CD$_4$O, δ_{ppm}): 8.81(s, 4H), 4.34(t, 4H), 3.52(t, 4H), 3.46(s, 4H), 3.18(s, 12H), 2.32(m, 4H), 1.38(2, 6H); Anal. Calcd for [$C_{28}H_{38}Br_2N_4O_4$]: C, 51.39; H, 5.85; Found: C, 49.61; H, 5.98; ESI-MS (*m*/*z*): calcd for [$C_{28}H_{38}Br_2N_4O_4$-2Br]$^{2+}$ and [$C_{28}H_{38}Br_2N_4O_4$-Br]$^{+}$: 247.1 and 575.2; Found 247.6 and 575.1.

2. Device fabrication

Fabrication of the conventional structure devices: The devices structure is ITO/PEDOT:PSS/Active layer/CIL/Al. The ITO-coated glass substrates were pre-cleaned ultrasonically in water/detergent, water, acetone, and isopropanol in sequence for 15 min. After 20 min of ultraviolet-ozone treatment, PEDOT:PSS was spin-coated on the ITO glasses, and the ITO substrates were dried in an oven at 150 °C for 15 min. The PBDB-T-2F: IT-4F (1:1, w/w) blend was dissolved in chlorobenzene (CB) with a concentration of 10 mg/ml (for polymer), with 1,8-diiodooctane (DIO) (0.5% by volume) as additive. The solution was stirred for 8 hours at room temperature and then spin-coated on the surface of PEDOT:PSS layer in nitrogen-based atmosphere glove box, and the optimal film of the active layer is ca. 100 nm. The active layer was then thermal annealed for 10 min at 100 °C. After spin-coating the active layer solutions, CIL methanol solution was spin-coated at 3000 rpm on the active layer. Finally, about 100 nm-thick Al was deposited onto the active layer under high vacuum of ~1× 10^{-5} Pa, giving an effective cell area of 3.70 mm^2. The *J*-*V* curves of the devices were measured under 100 mW cm^{-2} of the standard AM 1.5G spectrum.

Fabrication of the inverted structure devices: The devices structure is ITO/CIL/Active layer/MoO$_3$/Al. The ITO-coated glass substrates were washed as the conventional structure. The CIL methanol solution were spin-coated on the substrates and annealed at 150 °C for 15min in the air. The active layers were spin-coated as the conventional structure. Finally, 10 nm thick of MoO$_3$ and 100 nm thick of Al layer were deposited onto the active layer under high vacuum of ~1× 10^{-5} Pa.

Fabrication of the electron-only devices: The devices structure is ITO/ZnO/NDI-N or

NDI-Br/Al. The ITO-coated glass substrates were washed as mentioned above. The sol-gel ZnO were spin-coated on the ITO substrates and annealed at 200 °C for 1 hour in the air. IT-4F was dissolved in chloroform (20 mg/mL) and was spin-coated on the ZnO film. Afterwards, NDI-N or NDI-Br methanol solution was spin-coated as the conventional structure. Finally, 100 nm thick of Al layer were deposited onto the active layer under high vacuum of ~1× 10^{-5} Pa.

Fabrication of the 1.0 cm^2 all-printed device: The devices structure (ITO/PEDOT:PSS/Active layer/CIL/Al) is the same as that used in the spin-coated devices. The ITO-coated glass substrates were washed as mentioned above. PEDOT:PSS was blade-coated on the ITO glasses, and was thermal annealed at 150 ºC for 15 min. Then, PBDB-T-2F:IT-4F (1:1, w/w) blend in CB solution was blade-coated to fabricate the photoactive layer. The active layer was then thermal annealed for 10 min at 100 °C, and afterwards, NDI-N CIL was blade-coated on the photoactive layer. Finally, about 100 nm-thick Al was deposited on the CIL under high vacuum of ~1× 10^{-5} Pa, giving an effective cell area of 1.0 cm^2.

3. Instruments and measurements

The *J-V* measurement was performed via the solar simulator (SS-F5-3A, Enlitech) along with AM 1.5G spectra whose intensity was calibrated by the certified standard silicon solar cell (SRC-2020, Enlitech) at 100mw/cm^2. The external quantum efficiency (EQE) was measured by Solar Cell Spectral Response Measurement System QE-R3011 (Enli Technology Co., Ltd.). UV-vis absorption spectra were measured by Hitachi UH4150 spectrophotometer. The EPR spectra were recorded at 298 K using a JES-FA200 ESR Spectrometer. The cyclic voltammograms (CV) measurements were recorded on a Zahner IM6e electrochemical workstation by using glassy carbon discs as the working electrode, Pt wire as the counter electrode, Ag/AgCl electrode as the reference electrode with a scanning rate of 20 mV/s in a 0.1 M tetrabutylammonium hexafluorophosphate (Bu_4NPF_6) solution, and the potential of Ag/Ag^+ reference electrode was internally calibrated by using ferrocene/ferroncenium (Fc/Fc^+) as the redox couple. The tapping mode Atom Force Microscopy (AFM) measurements were performed on a Nanoscope V (Vecco) AFM. The GIWAXS measurements were done with an X-ray energy of 10 keV and recorded with a Pilatus 2M detector. The final patterns shown here were generated through use of Igor Pro and a modified version of the NIKA package.